Fall 2016

Computational fluid dynamics (CFD) simulations of molten steel flow patterns and particle-wall adhesion in continuous casting of steels

Mahdi Mohammadi-Ghaleni

Department:

COMPUTATIONAL FLUID DYNAMICS (CFD) SIMULATIONS OF MOLTEN STEEL FLOW PATTERNS AND PARTICLE-WALL ADHESION IN CONTINUOUS CASTING OF STEELS

by

MAHDI MOHAMMADI-GHALENI

A THESIS

Presented to the Faculty of the Graduate School of the

MISSOURI UNIVERSITY OF SCIENCE AND TECHNOLOGY

In Partial Fulfillment of the Requirements for the Degree

MASTER OF SCIENCE IN MATERIALS SCIENCE AND ENGINEERING

2016

Approved by

Mohsen Asle Zaeem, Advisor
Jeffrey D. Smith
Ronald O'Malley

PUBLICATION THESIS OPTION

This thesis consists of following two articles, formatted in the style used by Missouri University of Science and Technology.

Paper I, pages 7-38, has been published in the journal of METTALURGICAL AND MATERIALS TRANSACTIONS B.

Paper II, pages 39-60, has been published in the journal of METTALURGICAL AND MATERIALS TRANSACTIONS B.

ABSTRACT

In this research, the measurements of clog deposit thickness on the interior surfaces of a continuous casting nozzle were compared with Computational Fluid Dynamics (CFD) predictions of melt flow patterns and particle-wall interactions to identify the mechanisms of nozzle clogging. A hybrid turbulent approach, Detached Eddy Simulation (DES), was configured to simulate both turbulent structures and particle-wall interactions inside the nozzle accurately. For experimental measurements of nozzle clogging, a nozzle received from industry was encased in epoxy and carefully sectioned to allow measurement of the deposit thickness on the internal surfaces of the nozzle. CFD simulations of melt flow patterns and particle-wall adhesion inside the nozzle were performed applying the geometry and operating conditions of the industrial test. The simulation results indicated that the hybrid DES model incorporates both advantages of Reynolds Averaged Navier-Stokes (RANS) and Large Eddy Simulation (LES) models which are suitable for modeling wall bounded and transient turbulent flows, respectively. Also, the CFD results showed that the convergent areas of the interior cross section of the nozzle increased the velocity and turbulence of the steel flow inside the nozzle, and decreased the clog deposit thickness locally in those areas. The simulations predicted a higher rate of attachment of particles in the divergent area between two convergent sections of the nozzle, which matched the observations made in the industrial nozzle measurements. Additionally, a mathematical model is proposed for adhesion of particles, to the nozzle wall. This model provides a particle-wall adhesion criterion by considering the presence of external forces, physical characteristics of both wall and particle (e.g. hardness, Young's modules), and the effect of internal forces (e.g. Van Der Waals).

ACKNOWLEDGMENTS

Firstly, I would like to express my sincere gratitude to my advisor Prof. Mohsen Asle Zaeem for the continuous support of my study, for his patience, motivation, and immense knowledge. His guidance helped me in the time of research and writing of papers.

Besides, I would like to thank my thesis committee: Prof. Jeffrey D. Smith and Prof. Ronald O'Malley for their supports and insightful comments and encouragements.

My sincere thanks also goes to Dr. Chukwulebe and Dr. Bhattacharya, who provided me an opportunity to join ArcelorMittal Global R&D as an intern, and who gave access to the laboratory and research facilities.

I thank my friends and labmates, Mohsen, Ebrahim, Jake, Nihal, Leiren, Arezoo, Ning, and Avik for the great and helpful discussions, and for all the fun we have had in the last two years.

Last but not the least, I would like to thank my beautiful spouse, Elaheh, and my parents for providing me with unfailing support and continuous encouragement throughout my study and through the process of researching. This accomplishment would not have been possible without them.

TABLE OF CONTENTS

LIST OF ILLUSTRATIONS

Page

SECTION

PAPER I

PAPER II

SECTION

LIST OF TABLES

Page

SECTION

1. INTRODUCTION

1.1. CONTINUOUS CASTING OF STEEL

Currently, about 95% of steel casting process is performed continuously because of its low cost, high efficiency, and capability of producing steel in a vast variety of shapes and sizes [1]. The continuous casting process relies on many mechanical, thermal, chemical, and hydrodynamic processes [2]. The process mainly is based on pouring molten steel from a ladle into a tundish after which it goes into the mold through Submerged Entry Nozzle (SEN). The SEN (we name nozzle for simplification) is the most important part in every continuous caster process [3]. The main role of the nozzle is to prevent molten steel from oxidation, decrease emulsification of the top surface of the mold, and reduce air absorption during the casting process [4]. The flow patterns of molten steel leaving the nozzle out ports also have significant effects on molten steel solidification patterns inside the mold.

There are many factor having significant influences on melt flow pattern inside the nozzle out ports, such as flow patterns inside the nozzle, internal diameter of the nozzle, angle of out ports, opening size and shape of out ports, number of out ports, and nozzle bottom design [5]. Steel flow is directed into the mold by the nozzle out port jets at desired angles, with various levels of turbulence and swirl [6, 7]. The flow rate is usually controlled by either a stopper rod or slide gate imposing limitation to the opening area [7]. In the mold region, molten steel freezes against water-cooled copper walls to form a solid shell [1]. Hence, the quality of produced steel depends on the transport phenomena occurring in both the nozzle and mold [6]. Figure 1.1 presents a schematic view of a continuous casting process.

Steel flow usually contains solid inclusions/particles with different shapes and sizes which may adhere to the nozzle wall and create nozzle clogging. This clogging affects flow patterns and consequently can cause surface defects in the final produced steel. In the following section, nozzle clogging and its causes will be introduced.

Nozzle clogging is a universal serious problem in continuous casting of steels directly affecting the quality of steel produced. Nozzle clogging is caused by deposition of micro-inclusions present in the molten steel onto the nozzle wall [8]. Typically, removing these inclusions from the molten steel is very difficult, because: a) small particles have no tendency to form clusters and float-out, and b) there are various sources for additional inclusion formation such as precipitation during molten steel solidification process and particles formation due to steel re-oxidation in both the ladle and tundish [4, 9-11].

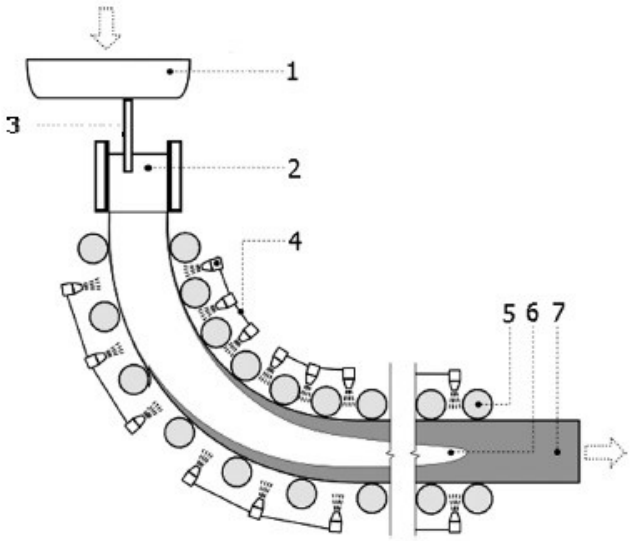

Figure 1.1. Schematic of a continuous caster [12]: 1-Tundish; 2-Mold; 3-SEN; 4-Coolant Nozzles; 5-Roller; 6-liquid Steel; 7-Solid Steel.

The interaction between inclusions and nozzle walls can be categorized into three different mechanisms:

- Chemical reactions between refractory and impurities present in both molten steel and nozzle wall
- Inclusions/particles created by erosion of the internal surface of the nozzle
- Deposition of inclusions/particles on the internal surface of the nozzle

Among several phenomena which may cause nozzle clogging, coalescence of inclusions formed by de-oxidation of products such as Al, Zr, and Ti oxides is the most dominant mechanism. In most of the times, once an inclusion adheres to the nozzle wall, it cannot be washed by molten steel flow because of presence of low velocity layers close to the walls. however, very small particles can be adhered to the area even with high flow rates depending on the surface tension, external forces, sintered bonds between particles and nozzle wall, as well as between particles. Once the first particle sticks to the nozzle wall, other particles are able to sinter and make an irregular network. These irregular networks later can be detached by the melt flow and turbulence, and be carried to the mold which make quality problems.

1.2. CONSEQUENCES OF NOZZLE CLOGGING

- *Reducing productivity of the process:* since continuous casting should ideally be steady state, once clogging occurs, the control system tries to compensate by opening the slide-gate or stopper rod to prevent a drop in mold level or as decrease in casting speed. If clogging continues, the control system can no longer compensate, and the productivity decreases.
- *Increasing casting cost:* if clogging occurs inside the nozzle, we should replace the nozzle, tundish, and even shutting down the continuous production which impose additional costs [13].
- *Creating quality problems:* when particles agglomerate on the nozzle wall, they can cause quality issues of produced steel. Nozzle clogging changes molten steel flow patterns in both the nozzle and mold. Also, some particle clusters may be dislodged from the nozzle wall, and then trapped in the produced steel creating quality problems [13, 14].

1.3. POSSIBLE METHODS IN ANALYZING NOZZLE CLOGGING

The molten steel flow patterns as well as geometry of the nozzle are one of the most important factors bringing the inclusions to the nozzle wall [4, 9-11]. According to some theories explaining the causes of adhesion of particles to the nozzle wall, it is found that the oxidized particles can be transported to the walls by turbulent and recirculating

flows [4, 9-11]. There are three different ways to analyze melt flow patterns and other phenomena occurring inside the continuous casting process:

- *Direct experimental method:* Performing continuous casting experiments in the actual process to obtain the most accurate results. However, completing such experiment can be difficult and very expensive, because continuous casting is a very high temperature process. Moreover, since the nature of the nozzle and mold usually are opaque, it is hard to observe what phenomena are occurring inside the system [15].
- *Physical models (Plexiglas-water mold):* Transparency is the most significant advantage of this method, which makes it possible to observe phenomena occurring inside the system. However, this method also can be expensive and inflexible, because the Plexiglas-water model should be only used when the Froude and Reynolds numbers of the experiment and real continuous casting process are the same. Using this method necessitates applying full scale models which makes it expensive because it can only be applied to one specific process condition [15].
- *Computational methods:* Arrival of modern computers has enabled us to computationally investigate the phenomena occurring inside almost any process such as continuous casting of steels. It provides us a great deal of detailed information such as flow field, inclusion transport and path line, phases transformation, solidification, and mobility of particles in any desired location with the most affordability and flexibility [15]. There are different computational methods at different length scales which are potentially applicable to study different phenomena related to nozzle clogging. To date, Computational fluid dynamics (CFD) has been the most popular method for investigating melt flow patterns, turbulence, and particle behavior inside the continuous casting process. In following, we briefly introduce CFD method, as well as it advantages and limitations.

1.4. COMPUTATIONAL FLUID DYNAMICS (CFD)

CFD is a combination of three particular fields; fluid dynamics, mathematics, and computational programming. In the past years, experts wrote their own program to solve equations that represent the actual process. With the increase demands from industries and academia to solve and process the problems in a shorter time, it is not surprising that

commercial software packages have been developed to respond the demands. Currently, CFD has become a very powerful tool to be used either for industrial or research applications. Computational simulation and analyses have been performed in many fluid engineering applications such as aerospace, automotive, biomedical, chemical and material, civil, environmental and power engineering. If we ponder the planet we live in, almost everything revolve or move within a fluid [16].

1.4.1. Advantages of CFD.

- *Relatively low cost:* Sometimes, it is very expensive to perform physical experiments to get empirical data. On the other hand, CFD simulations are relatively inexpensive and the cost of simulation decreases once the computers become more powerful. It also offers ability to solve a range of complicated flow problems cost-effectively where the analytical approach is lacking.
- *High speed:* CFD simulations can be done in a short period of time, and also quick turnaround means engineering data can be defined early in the design process.
- *Capability in simulating complex phenomena:* Many flow and transfer phenomena such as hypersonic flows cannot be easily examined experimentally, yet CFD provides the ability of simulating any physical condition theoretically.
- *Ability to simulate ideal conditions:* CFD is able to have a great control specific phenomena in a study. For instance, a heat transfer process can be idealized with adiabatic, constant heat flux, or constant temperature boundaries.
- *Availability of comprehensive information*: Experiments only permit us to collect data from a limited number of locations in a system, but CFD allows us to examine results from a large number of locations, and to easily plot this results to visualize them [17].

1.4.2. Limitation of CFD. Solutions rely upon physical models and real world processes such as turbulence, compressibility, chemistry, multiphase flow etc. So, its results only can be as accurate as the defined physical models. CFD have some limitations:

- *Numerical errors:* solving equations by computer may introduce several numerical errors. For instance, some of the errors are:

1- Round-off error due to finite word size available in the computer

2- Truncation error due to approximations in the numerical models. This kind of error will approach zero as the grid is refined, so mesh refining is one way to deal with truncation errors [17].
3- Hardware limitations: in spite of remarkable progresses in introducing new more powerful computer hardware to the world, some of computers still are not enough fast for doing thousands of calculations needed for multiphase flows including chemical reactions [16].
4- Boundary conditions: the accuracy of the CFD solution also depends on both initial and boundary conditions introduced to the numerical model. For example, if a flow is entered to the domain by a pipe, we should use a fully developed profile for velocity rather than uniform velocity assumption [17].

PAPER

I. COMPUTATIONAL FLUID DYNAMICS STUDY OF MOLTEN STEEL FLOW PATTERNS AND PARTICLE-WALL INTERACTIONS INSIDE A SLIDE-GATE NOZZLE BY A HYBRID TURBULENT MODEL

(Published in Metallurgical Materials Transaction B, 2016)

Mahdi Mohammadi-Ghaleni, Mohsen Asle Zaeem*, Jeffrey D. Smith, and Ronald O'Malley

Department of Materials Science and Engineering, Missouri University of Science and Technology, 1400 N. Bishop Ave, Rolla, MO 65409, USA

ABSTRACT

Melt flow patterns and turbulence inside a slide-gate throttled submerged entry nozzle (SEN) were studied using Detached-Eddy Simulation (DES) model, which is a combination of Reynolds-Averaged Navier-Stokes (RANS) and Large-Eddy Simulation (LES) models. The DES switching criterion between RANS and LES was investigated to closely reproduce the flow structures of low and high turbulence regions similar to RANS and LES simulations, respectively. The melt flow patterns inside the nozzle were determined by k-ε (a RANS model), LES, and DES turbulent models, and convergence studies were performed to ensure reliability of the results. Results showed that the DES model has significant advantages over the standard k-ε model in transient simulations and in regions containing flow separation from the nozzle surface. Moreover, due to applying a hybrid approach, DES uses a RANS model at wall boundaries which resolves the extremely fine mesh requirement of LES simulations, and therefore it is computationally more efficient. Investigation of particle distribution inside the nozzle and particle adhesion to the nozzle wall also reveals that DES model simulations predicts more particle-wall interactions compared to LES model.

Keywords: Computational Fluid Dynamics, Detached-Eddy Simulation (DES), Large Eddy Simulations (LES), Submerged Entry Nozzle (SEN).

---

* Corresponding author: Tel.: +1 573 341 7184; fax: +1 573 341 6934.

E-mail address: zaeem@mst.edu (M. Asle Zaeem).

1. INTRODUCTION

Currently about 95% of steel products are manufactured through continuous casting because of its low cost and high efficiency, as well as its capability of manufacturing steel products with different shapes and sizes [1]. During continuous casting, molten steel is poured from a ladle into a tundish, and then is directed into a copper mold by a submerged entry nozzle (SEN) at a desired angle and with various levels of turbulence and swirl [2, 3]. Melt flow patterns inside the SEN and characteristics of out port jets have significant effects on steel solidification patterns as well as on the size and shape of inclusions inside the mold, which affect the quality of steel products [2].

The continuous casting process relies on many physical, mechanical, thermal and chemical phenomena which are very complex [4]. One of the most frequent undesired phenomenon affecting the continuous casting is nozzle clogging, which is caused by deposition and sintering of micro-inclusions onto the SEN walls [5]. There are several undesired consequences associated with nozzle clogging, such as reduced productivity, increased casting costs, and degradation of the quality of the steel produced [6]. Computational Fluid Dynamics (CFD) has been one of the most popular methods for studying melt flow patterns and inclusion behavior in continuous casting systems [7]. This approach is widely used, because continuous casting is a very high temperature process, ~1900K (1627C), so conducting steel-flow experiments at such temperatures is very difficult. Also, because of the opaque nature of the SEN material, it is difficult to observe melt flow patterns and particle behavior inside the actual SEN. This issue can be also resolved by using Plexiglas-water model system, in which it is easy to observe and measure the desired phenomena and parameters, however, the Reynolds and Froud numbers of the water model should be similar to those of the actual process [8]. This means that for different casting processes, different water models need to be constructed which may be expensive. Hence, CFD is considered a reliable alternative method to study flow patterns and improve processes efficiency with a lower cost [3, 7-19].

Since continuous casting is a highly turbulent process, applying a suitable turbulent model is necessary to accurately and efficiently study the melt flow patterns and inclusion/particle behaviors in the process. Most of the previous work on CFD simulations

of melt flow patterns in the continuous casting process have utilized Reynolds-Averaged Navier-Stokes (RANS) turbulent models (especially the k-ε model) to simulate flow turbulence [17-22]. For instance, Thomas et al. [18, 19] studied the effects of nozzle design and process parameters on the molten steel flow patterns and turbulence inside an SEN using the k-ε model. Bai et al. [17] and Zhang et al. [22] used the k-ε model to study the effect of nozzle clogging on the flow patterns by manually adding clogged parts to the geometry of the SEN. Their results indicated that clogging buildup strongly affects melt flow patterns in the nozzle as well as the mold. Pfeiler et al. [20] investigated the effects of argon gas bubbles and inclusions on the molten steel flow behavior. They compared one-way (flow affects particle movement, not vice versa) and two-way coupling of inclusions/bubbles with molten steel. Their results showed that inclusions and bubbles, whose transport highly depends on their size and density, were dispersed more with two-way coupling. Therefore, they concluded that considering two-way coupling is essential for proper prediction of inclusion/bubble behavior in CFD simulations. In 2001, Thomas et al. [23] compared the k-ε and large eddy simulation (LES) models to show flow turbulence inside the mold in transient and steady state conditions. They realized that the k-ε model is capable of predicting the melt flow in steady state conditions reasonably well, yet it has difficulties in handling flow turbulence in transient simulations. LES model simulations predicted the melt flow patterns and turbulent areas very well in transient conditions.

Recently LES model has become very popular among CFD researchers to simulate flow patterns in the continuous casting process [3, 10, 14, 19, 23-27], because of its accuracy in transient simulations compared with RANS models. For instance, Yuan et al. [3, 14] applied LES approach to study melt flow and particle distribution inside a continuous caster mold. They presented three simulation results to identify the difference between full-pool and symmetric half-pool, also between a full-scale water mold and real steel-caster behavior. Particle motion and distribution inside the mold along with particles captured by the mold solidification front also were studied. Chaudhary et al. [24] compared the results of transient turbulent flow in a continuous caster using LES and k-ε turbulent models with experimental measurements. Their results indicated that, compared to k-ε

model simulations, simulation of turbulence using LES model was better matched to the experimental measurements.

Although LES models have shown accuracy in simulating turbulent flow structures at transient conditions, they do have some limitations in simulating wall bounded flows [13]. LES adjusts the length of the turbulence by fluid friction velocity and viscosity within the viscous sublayers on the wall. Hence, it requires a high number of grid points to resolve the near-wall flow structures accurately [15, 28]. In the case of having a highly turbulent process, the thickness of viscous sub-layer decreases, and so the model demands extremely fine mesh within the viscous sub-layers. It has been shown that the number of grid points required for LES model to resolve wall-flow interactions scales as $O\left(\mathrm{Re}_{\tau}^{2}\right)$, where Re_{τ}^{2} is the friction velocity-based Reynolds number [15]. As a result, LES is only recommended for simulation of fluid flows where either the effect of wall boundary layers are not important or the boundary layers are laminar due to the low Reynolds number [12, 13].

The objective of this paper is to simulate melt flow patterns and particle distribution inside a slide-gate nozzle using a hybrid turbulent model, DES, and then compare the results with k-ε and LES simulations results. DES approach comprises both advantages of LES and RANS models. The main idea is to apply a RANS model for near-wall layers, and LES model for the detached zones and regions far away from the wall [29]. This approach resolves the issues associated with LES model in simulating internal flows, and therefore decreases the LES demand of extremely fine mesh elements at wall boundary layers. In this study, the results of DES model have been compared with standard k-ε and LES-WALE simulation results.

This paper contains four sections; Section 2 presents the mathematical equations for the melt flow patterns, inclusions/particles movement, and turbulence inside the nozzle. Section 3 and Section 4 illustrate the simulation procedure and results, respectively. Finally, Section 5 presents a brief conclusion about the simulation results.

2. GOVERNING EQUATIONS

The Eulerian-Lagrangian approach was applied for a mixture of molten steel and inclusions/particles inside the system. This method uses Eulerian approach to simulate melt flow patterns, and Lagrangian technique to track particles inside the nozzle. This section presents the mathematical modeling of the process based on following assumptions:

- Every particle which touches the wall will be attached to it.
- Steel behaves as an incompressible Newtonian fluid.
- The temperature of the system is isothermal.
- Solidification of steel does not occur.
- The roughness of nozzle wall is zero.

The 3D continuity Navier-Stokes (NS) equations for an incompressible Newtonian fluid were solved to model the melt flow patterns inside the nozzle. These equations are based on the mass conservation and momentum equations at every point in the computational domain [30]. The general conservation equation contains a general variable, ϕ, by which a balance between various processes within a finite control volume is made. The momentum, continuity, and turbulence equations can be derived from the following general equation [11, 31]:

$$\frac{\partial}{\partial t}(\rho\phi)+\frac{\partial}{\partial x_i}(\rho U_i\phi)=\frac{\partial}{\partial x_i}\left(\Gamma_\phi\frac{\partial\phi}{\partial x_i}\right)+S_\phi, \tag{1}$$

where the first and second terms on the left side are changes of ϕ with time and transport due to convection, respectively; ρ is density of molten steel, t is the time, x_i represents coordinate directions (x, y or z), and U_i is velocity of molten steel at i direction. The first term on the right side states the transport due to diffusion, where Γ_ϕ is the diffusion coefficient. The second term on the right side of equation (1) presents the source term which can be added based on a specific process condition.

2.1. TURBULENT MODELS

Turbulence is one of the most important factors that has significant effects on melt flow patterns and particle behavior in the system. The equations of three turbulent models, standard k-ε, Shear Stress Transport (SST), LES and DES, are presented in this section.

The standard k-ε model. The standard k-ε model consists of two equations following the same format as equation (1) [19]. Kinetic energy equation (k) is:

$$\frac{\partial(\rho k)}{\partial t}+\frac{\partial}{\partial x_i}(\rho U_i k)=\frac{\partial}{\partial x_i}\left[\left(\mu+\frac{\mu_t}{\sigma_k}\right)\frac{\partial k}{\partial x_i}\right]+P_k+P_{kb}-\rho\varepsilon+S_k, \tag{2}$$

and dissipation rate equation (ε) is:

$$\frac{\partial(\rho\varepsilon)}{\partial t}+\frac{\partial}{\partial x_i}(\rho U_i \varepsilon)=\frac{\partial}{\partial x_i}\left[\left(\mu+\frac{\mu_t}{\sigma_\varepsilon}\right)\frac{\partial \varepsilon}{\partial x_i}\right]+\frac{\varepsilon}{k}\left(C_{\varepsilon 1}P_k-C_{\varepsilon 2}\rho\varepsilon+C_{\varepsilon 1}P_{\varepsilon b}\right)+S_\varepsilon, \tag{3}$$

where $C_{\varepsilon 1}$, $C_{\varepsilon 2}$, σ_k, σ_ε are constants equal to 1.44, 1.92, 1 and 1.3, respectively [10, 32]. S_k and S_ε are the source terms for turbulent kinetic energy and dissipation rate, respectively. μ and μ_t are molten steel and turbulence viscosity, respectively. Turbulence viscosity is linked to the turbulent kinetic energy and dissipation rate by following relation:

$$\mu_t=\rho C_\mu\frac{k^2}{\varepsilon}, \tag{4}$$

where C_μ is a constant equal to 0.09 [10, 32].

P_{kb} and $P_{\varepsilon b}$ in equations (2) and (3) take into account the influence of buoyancy forces for turbulent kinetic energy and dissipation rate, respectively. P_k is the turbulence production due to viscous forces. For incompressible flows, it can be defined as:

$$P_k = \mu_t \left(\frac{\partial U_i}{\partial x_j} + \frac{\partial U_j}{\partial x_i} \right) \frac{\partial U_i}{\partial x_j} . \tag{5}$$

2.1.1. LES Model. The logic behind the LES model is to separate the large and small eddies in the computational domain. The equations for LES model are governed by filtering time-dependent NS equations. LES filters eddies whose scale are smaller than the filter width and grid spacing used in the domain. For instance, the filtered momentum equation for an incompressible flow can be derived from equation (1) as follows [27, 33]:

$$\frac{\partial \bar{U}_i}{\partial t} + \frac{\partial}{\partial x_j}\left(\bar{U}_i \bar{U}_j\right) = -\frac{1}{\rho}\frac{\partial \bar{p}}{\partial x_j} + \frac{\partial}{\partial x_j}\left[\nu\left(\frac{\partial \bar{U}_i}{\partial x_j} + \frac{\partial \bar{U}_j}{\partial x_i}\right)\right] - \frac{\partial \tau_{ij}}{\partial x_j}, \tag{6}$$

where $\bar{U}_i$ and $\bar{U}_j$ are the velocity components at x_i and x_j directions, respectively. The over-bar indicates an averaged quantity. ν represents the kinematic viscosity, and τ_{ij} also is the subgrid-scale stress, defined by:

$$\tau_{ij} = \overline{U_i U_j} - \bar{U}_i \bar{U}_j . \tag{7}$$

LES model solves large scale turbulent structures directly, however the effect of the small scales is taken into account by appropriate subgrid-scale (SGS) models. An eddy viscosity methodology also relates the subgrid-scale stresses, τ_{ij}, to the large scale strain tensor, $\bar{S}_{ij}$, according to these equations:

$$-\left(\tau_{ij} - \frac{\delta_{ij}}{3}\tau_{kk}\right) = 2\nu_{SGS}\bar{S}_{ij}, \tag{8}$$

$$\bar{S}_{ij} = \frac{1}{2}\left(\frac{\partial \bar{U}_i}{\partial x_j} + \frac{\partial \bar{U}_j}{\partial x_i}\right), \tag{9}$$

where τ_{kk} is the isotropic part of the subgrid-scale stresses, and ν_{SGS} represents small scale of subgrid-scale viscosity. Three models, WALE, Smagorinsky, and Dynamic Smagorinsky-Lilly, have been introduced to define ν_{SGS} for the LES approach. The equations for these models can be found elsewhere [34-37]. The WALE model has been applied in this work to define ν_{SGS} in LES simulations [26].

2.1.2. DES Model. DES is a hybrid turbulent model switching between RANS and LES models in the computational domain. DES is a combination of transformed forms of k-ε, k-ω and LES models in which the combination of k-ω and k-ε models is called the SST model [26, 32]. For this reason, DES is known to switch between SST and LES models. In the following section, the SST methodology is described, and then the DES approach (based on SST and LES models) is explained.

SST part of DES model

In addition to a transformed form of k-ε model (Section 2.1), SST uses k-ω model to predict flow turbulence in the computational domain. The two governing equations for k-ω [28, 32] are the kinetic energy equation (k):

$$\frac{\partial(\rho k)}{\partial t}+\frac{\partial}{\partial x_i}(\rho U_i k)=\frac{\partial}{\partial x_i}\left[(\mu+\sigma_k\mu_t)\frac{\partial k}{\partial x_i}\right]+\tau_{ij}S_{ij}-\beta'\rho k\omega, \tag{10}$$

and the turbulent frequency equation (ω):

$$\begin{aligned}&\frac{\partial(\rho\omega)}{\partial t}+\frac{\partial}{\partial x_i}(\rho U_i\omega)=\\&\frac{\partial}{\partial x_i}\left[(\mu+\sigma_\omega\mu_t)\frac{\partial\omega}{\partial x_i}\right]+\alpha\rho S_{ij}{}^2-\beta\rho\omega^2+2(1-F_1)\rho\sigma_{\omega 2}\frac{1}{\omega}\frac{\partial k}{\partial x_i}\frac{\partial\omega}{\partial x_i},\end{aligned} \tag{11}$$

where S_{ij} is the strain rate, and α, and β' are constants equal to 0.55, and 0.09, respectively. The turbulent model closures are σ_k and σ_ω, which change when the SST model switches between k-ε and k-ω. This means, if the SST model is operating in k-ε

mode, $\sigma_k = \sigma_{k1} = 0.85$, $\sigma_\omega = \sigma_{\omega 1} = 0.65$, and $\beta = \beta_1 = 0.075$. However, if the SST model is working in k-ω mode, $\sigma_k = \sigma_{k2} = 1$, $\sigma_\omega = \sigma_{\omega 2} = 0.856$, and $\beta = \beta_2 = 0.0828$ [10, 32, 38].

SST uses two blending functions to incorporate the switching between the two models based on the distance from the wall (*y*). The first blending function is:

$$F_1 = \tanh\left\{\left\{\min\left[\max\left(\frac{\sqrt{k}}{\beta^{'}\omega \mathrm{y}}, \frac{500\nu}{y^2\omega}\right), \frac{4\rho\sigma_{\omega 2}k}{CD_{k\omega}y^2}\right]\right\}^4\right\}, \tag{12}$$

where $CD_{k\omega}$ is defined as:

$$CD_{k\omega} = \max\left(2\rho\sigma_{\omega 2}\frac{1}{\omega}\frac{\partial k}{\partial x_i}, 10^{-10}\right). \tag{13}$$

F_1 is equal to 1 inside the wall boundary layers, where the last term in equation (2.11) becomes zero. In this condition, the SST uses k-ω model because of its accuracy in handling wall-flow interactions. Away from the surfaces, F_1 decreases from 1 to 0 where k-ε is used.

A limiter is applied to control the over prediction of the eddy-viscosity at boundary layers. Accordingly, the eddy-viscosity, ν_t, is defined by:

$$\nu_t = \frac{\mu_t}{\rho} = \frac{\alpha_1 k}{\max\left(\alpha\omega, S_{ij}F_2\right)}, \tag{14}$$

where α_1 is a constant equal to 0.31 [38], and F_2 is the second blending function of the DES model. F_2 is similar to F_1, and it restricts the limiter to the wall boundary layers:

$$F_2 = \tanh\left[\left[\max\left(\frac{2\sqrt{k}}{\beta^{'}\omega \mathrm{y}}, \frac{500\nu}{y^2\omega}\right)\right]^2\right]. \quad (15)$$

A turbulence production limiter is also applied by the SST model to prevent the build-up of turbulence in stagnant regions:

$$\tilde{P}_k = \min\left(P_k, 10.\rho\beta^{'}k\omega\right), \quad (16)$$

where P_k is calculated from equation (2.5).

DES hybrid approach

To construct a DES-type hybrid approach, a transformation should be adopted for the dissipation term existing in the turbulent kinetic energy equation (equation 10). Thus, after presenting a length scale (L_t), equation 10 can be rewritten as [28]:

$$\frac{\partial(\rho k)}{\partial t} + \frac{\partial}{\partial x_i}(\rho U_i k) = \frac{\partial}{\partial x_i}\left[(\mu + \sigma_{k1}\mu_t)\frac{\partial k}{\partial x_i}\right] + \tau_{ij}S_{ij} - \beta^{'}\rho k\omega F_{DES} \quad (17)$$

where F_{DES} is the blending function of DES model, defined as:

$$F_{DES} = \max\left(\frac{L_t}{C_{DES}\Delta}(1 - F_{SST}), 1\right), \quad (18)$$

In DES simulations, the stress tensor (τ_{ij}) is calculated by the LES-type Smagorinsky model [37].

While the DES model is applied, the SST part uses k-ω in the wall boundaries, and in the regions far away from the wall boundaries DES criterion selects between k-ε and LES [32]. The selection will be done by comparing the turbulent length scale, L_t, and Δ which is the maximum of element edge: in the zones where L_t is larger than multiplication

of DES constant (C_{DES}) and Δ (such that $C_{DES}\Delta < L_t$), the DES is operating in LES mode. But, when $C_{DES}\Delta > L_t$, then F_{DES} =1, the DES model is acting in k-ε mode [28].

From the view point of numerical treatment of the equations, DES model switches between RANS (k-ε or k-ω) and LES models to solve the equations, such that it uses second order upwind-biased scheme for RANS regions, and central difference scheme for LES regions [15, 32].

2.2. PARTICLE TRAJECTORY MODEL

Lagrangian approach was used to compute velocity equation for particles inside the nozzle. This approach considers a balance between drag, buoyancy, and other interfacial forces at every point. The balance equation is coupled with momentum and continuity equations using empirical interphase drag between molten steel and particles. The particle trajectory equation is defined as [39, 40]:

$$\frac{du_{pi}}{dt} = F_D + F_G + F_{VM} + F_P + F_B . \tag{19}$$

The first term, F_D , is the drag force per unit particle mass caused by the difference between the particle and fluid velocities:

$$F_D = \frac{18\mu}{\rho_p {d_p}^2} \frac{C_D Re_p}{24} \left(U_i - U_{pi} \right), \tag{20}$$

where ρ_p is particle density, and U_{pi} is particle velocity in *i* direction. C_D and Re_p are drag coefficient and particle Reynolds number, respectively [41]:

$$C_D = \begin{cases} \frac{24}{Re}\left(1 + \frac{1}{6} Re_p^{2/3}\right) & if\ Re_p < 1000 \\ 0.44 & if\ Re_p \geq 1000 \end{cases}, \tag{21}$$

$$\mathrm{Re}_P = \frac{\rho d_p \left| u_p - u \right|}{\mu_f}, \tag{22}$$

where *Re* is the melt Reynolds number.

The second term in equation (19), F_G, is the gravitational force:

$$F_G = \frac{\rho_p - \rho}{\rho} g \ , \tag{23}$$

where g is the gravitational force. F_{VM} is the virtual mass force due to the relative acceleration between the particle and the fluid [42]:

$$F_{VM} = \frac{1}{2} \frac{\rho}{\rho_p} \frac{d}{dt} \left(U_i - U_{pi} \right). \tag{24}$$

F_p is the force imposed on the particles by pressure gradient existing in the system:

$$F_p = \frac{\rho}{\rho_p} U_i \frac{\partial U_i}{\partial x_i} . \tag{25}$$

F_B is the buoyancy force which is caused by the difference between the fluid and particle densities:

$$F_B = \frac{\pi d_p^3}{6} \left(\rho_p - \rho \right) g \ . \tag{26}$$

The dispersion of particles due to turbulence inside the nozzle is considered using a stochastic tracking model, which considers the effect of instantaneous turbulent velocity fluctuations on tracking of particles [20]. The other forces on solid particles are negligible

for particles with the average diameter assumed in this research (d_p = 50 μm). For example, the lift force is not considered, because it is negligible for solid particles with the diameter less than 300 μm [40].

3. SIMULATION PROCEDURE

In following, the simulation steps, and boundary and initial conditions have been explained.

3.1. DOMAIN GEOMETRY AND MESH

CFD analyses were performed using ANSYS CFX 14.0. The geometry of the nozzle and finite volume mesh were built using design modeler and meshing of ANSYS, respectively. The computational domain contains the nozzle with actual dimensions conveying molten steel from tundish to mold. The nozzle consists of two parts, upper well nozzle and lower nozzle. Upper and lower nozzles are connected by a slide-gate which moves in 90° orientation compared to the direction of the SEN ports. Figure 3.1 shows the nozzle geometry and an example of mesh grids used for the simulations. Table 3.1 also specifies the nozzle dimensions and casting operating conditions used to perform the simulations [22].

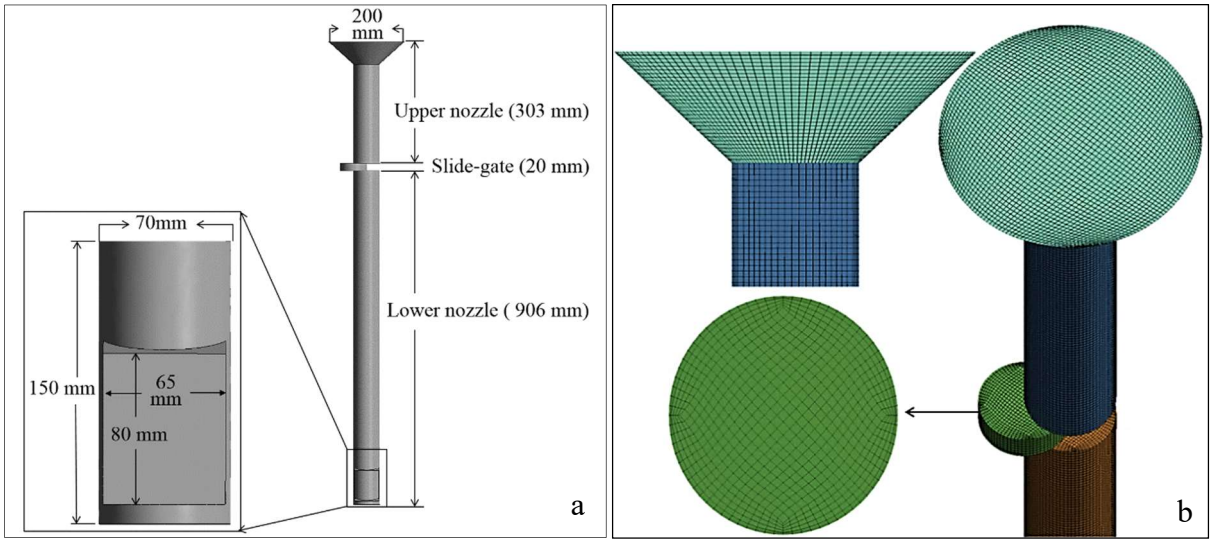

Figure 3.1. Nozzle geometry and dimensions (a), an example of mesh (b).

Table 3.1. Operating conditions used for simulations [22].

Parameter	Value	Parameter	Value
Nozzle bore diameter [mm]	70	Molten steel thermal conductivity [W/m k]	41
Out ports(width × height)[mm]	65 × 80	Density of Alumina particles [kg/m^3]	4,000
Port angle [Degree Down]	15	Number of particles	30,000
Up nozzle length [mm]	323	Casting temperature [K]	1,818
Total nozzle length [mm]	1,229	Steel thermal expansion coefficient [1/K]	0.0001
Slide-gate orientation [degree]	90	Diameter of tundish bottom well [mm]	200
Nozzle submerged depth [mm]	150	Inlet velocity [m/sec]	0.15
Viscosity of liquid steel [kg/m.sec]	0.0056	Inlet kinetic energy [m^2/sec^2]	0.000225
Density of liquid steel [kg/m^3]	7,021	Inlet dissipation rate [m^2/sec^3]	0.000338

3.2. INITIAL AND BOUNDARY CONDITIONS

Appropriate initial and boundary conditions are required in CFD simulations to have accurate solutions of continuity and momentum equations. A uniform normal velocity was assumed at the inlet, which is a reasonable assumption when a tundish is not included in the simulations and a fixed slide-gate position is considered. Moreover, turbulent dissipation rate and turbulent kinetic energy were defined at the inlet based on semi-empirical relations for pipe flows [24]. These relations are defined as:

$$\varepsilon = k^{1.5} / 0.05D \,, \tag{27}$$

$$k = 0.01 U_{in}^2, \tag{28}$$

where D and U_{in} are hydraulic diameter of the inlet plane and melt inlet velocity, respectively.

Particles (Al_2O_3) were added into the nozzle from the inlet plane, where 30,000 spherical particles were injected from random positions. The mean size of particles injected into the nozzle was 50 μm. In reality the size of particles (inclusions) may vary from a few microns to hundreds of microns.

The nozzle walls were considered to be non-slip walls during the simulations, and the roughness of the walls was assumed to be zero.

An averaged static pressure was assumed over the nozzle out ports, because the nozzle is submerged into the mold. This boundary condition allows the simulation to predict molten steel velocity in the nozzle out ports. Hence, the relative pressure at the nozzle out port was set using the static pressure relation:

$$P = \rho g h_s, \tag{29}$$

where h_s is submerged depth of the nozzle in the mold.

As initial conditions, the steady state simulation results were applied to LES and DES transient simulations.

4. SIMULATION RESULTS

This section presents the result of the CFD simulations.

4.1. CONVERGENCE STUDY

Convergence study is required to ensure that the simulation results are independent of mesh size. For this reason, different numbers of elements were used to check the convergence of simulation results. The time-averaged velocity of melt flow on a line located at the center of the nozzle (centerline) was used as a parameter for determining the optimum number of elements.

Figure 4.1 shows the time-averaged velocity of melt flow at the nozzle centerline predicted by LES model (geometry of the nozzle is included at the right side of the figure). According to the graph, average velocity at the nozzle centerline follows similar trends for cases with 1.8 million (M), 2.5 M and 3 M elements. However, once the number of elements decreases from 1.8 M to 1.6 M elements, some deviations of the velocity profile can be seen at the nozzle out ports and after the slide-gate. Therefore, 1.8 M elements were selected for LES simulations.

Figure 4.2 displays the time-averaged velocity at the nozzle centerline calculated by DES simulations in the case $F_{SST} = F_1$. It is clear that the trend of averaged velocity at the centerline does not change significantly once the number of elements increases from 1.6 M to 1.8 M elements. Therefore, 1.6 M elements were used to perform DES simulations in this case, which is only 12% less than that of the LES simulations to produce similar results. For the case $F_{SST} = F_2$, when a regional mesh refinement is used for flow separation regions (termed zonal-DES), a fine mesh is applied only after the slide-gate, and larger mesh is used for other regions decreasing the number of elements to about 1 M.

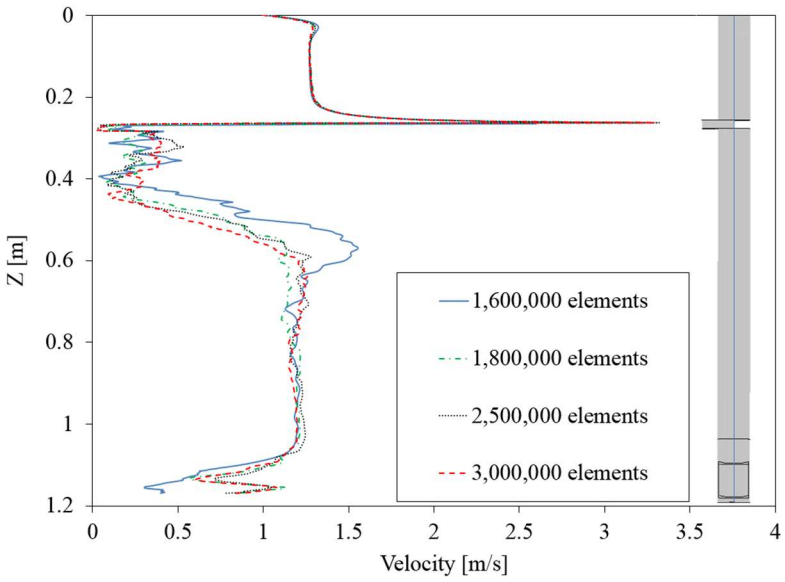

Figure 4.1. Time-averaged velocity of melt flow at centerline of the nozzle for LES model; simulation time: 2 seconds.

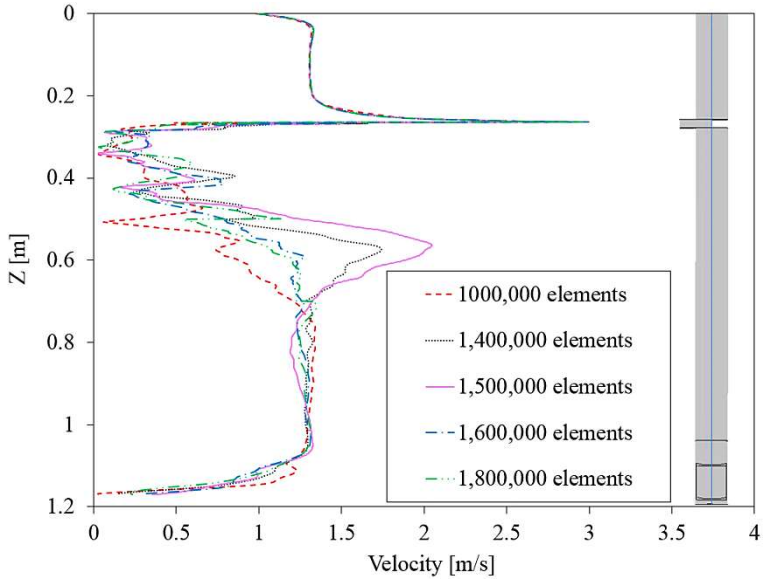

Figure 4.2. Time-averaged velocity of melt flow at centerline of the nozzle for DES model; simulation time: 2 seconds.

Time step plays a significant role in every LES and DES simulation, because it determines the quality of the turbulent structures resolution in the simulations [26].The time step for the transient simulations was selected to be 0.0001. It was observed that the simulations reach a quasi-steady state condition after 2 seconds. Hence, the simulations were performed for 20,000 time steps (2 seconds). The run time for the LES model was about 10 days using one computing node including 16 CPU cores (3.4 GHz) and 64 GB RAM. The same node needed 6 days to complete 2 seconds of zonal-DES simulations. Hence, for our case, zonal-DES was about 40% more efficient than LES in term of computational cost.

4.2. DES MODEL CALIBRATION

DES approach as mentioned earlier, switches between RANS and LES models to predict accurately the turbulent structures in the system. To ensure that a DES model is working properly, two factors should be monitored [16, 32]. First, it is important to ensure that DES blending function (F_{DES}) uses the LES model for detached and highly turbulent regions, and a RANS model for the other regions. Second, it is important to determine if the turbulent structures at flow separation regions (e.g. slide-gate) are similar to LES predictions [16].

Considering equation (18), F_{SST} can be set as F_1, F_2 or zero. At first, the simulations were completed using $F_{SST} = F_2$. In this case, DES applies the k-ω model to the wall regions, and either the LES or k-ε model to the other regions. For instance, if any flow separation occurs inside the system, DES should apply LES model in that region. Figure 4.3 shows the evolution of DES blending function at the center plane of the nozzle. This plot indicates that the DES model applies k-ε model at most regions inside the nozzle (red regions). This is not appropriate, because the k-ε model is not able to simulate accurately flow separation regions, turbulent structures, and fluctuations at transient condition. For the slide-gate 50% open, the gate acts similar to an obstacle inside the melt flow stream, causing flow separation. Therefore, it is required to calibrate the DES model such that the turbulent structures can be simulated accurately in flow separation regions. This can be achieved by applying the LES model in those regions. To resolve the switching issue, several tests such as reducing time steps, applying finer mesh grids, and changing the

blending function of the SST model were considered. The use of smaller time steps for the simulations (less than 0.0001s) did not resolve the issue.

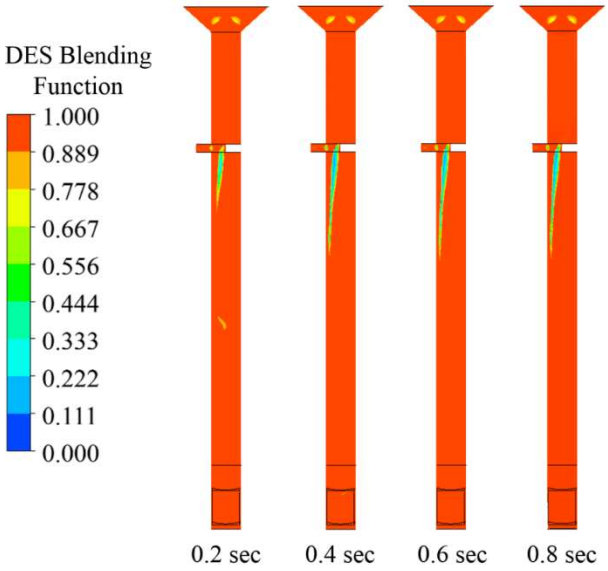

Figure 4.3. Contours of DES blending function at center-plane of the nozzle; $F_{SST} = F_2$. A uniform mesh was used for the entire nozzle. Red and blue colors show areas where k-ε and LES models are activated, respectively.

Another way to resolve the switching issue is to change the blending function of RANS model from F_2 to F_1 ($F_{SST} = F_1$). This solution method deactivates the k-ε in the DES model, which means that the DES model is forced to use k-ω in the wall boundary layers and LES in the other regions [32]. Figure 4.4 displays the evolution of DES blending function for this case. It can be seen that after 0.8 seconds of simulation, almost the entire domain is covered by the LES model (blue regions), except the wall boundaries which are covered by the k-ω model. This case shows similar results to the LES simulations; however, it is not an efficient way to use the hybrid DES model as it should be configured appropriately to apply the LES model in flow separation and highly turbulent regions, only.

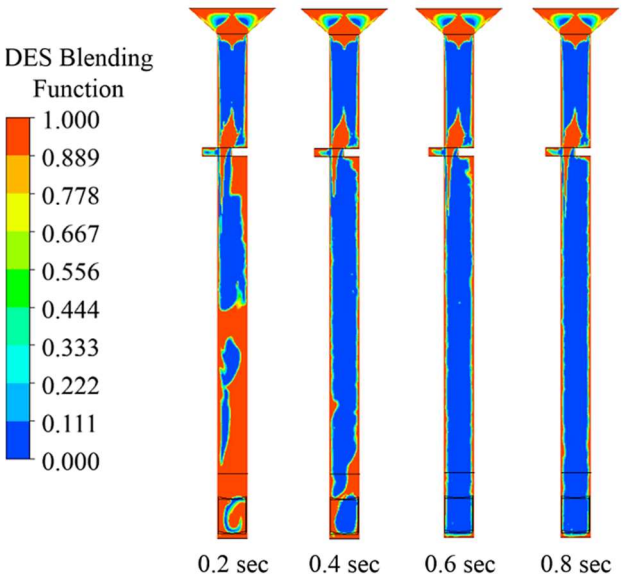

Figure 4.4. Contours of DES blending function at the center-plane of nozzle; $F_{SST} = F_1$. A uniform mesh was used for the entire nozzle (same as in Figure 4.1). Red and blue colors show areas where k-ε and LES models are activated, respectively.

Another way to resolve the switching issue of the DES model is to refine the mesh in regions with expected flow separation (e.g., after the slide-gate). According to Section 2.1.2, when $C_{DES}\Delta < L_t$, the LES model should be activated. Hence, a mesh refinement in that particular region makes the DES model to switch to LES (zonal-DES [32]). Subsequently, the mesh refinement was done for the region after the slide-gate based on the flow turbulence structures observed in LES simulations (~25 cm after slide-gate). Subsequently, the DES blending function was changed to $F_{SST} = F_2$, and then several simulations using different mesh size for separation regions were completed to observe a reasonable switching for the DES model. The element sizes for other regions were kept the same size as RANS models (larger that the mesh size in LES model), because the DES model will apply a RANS model (k-ε) in those regions. Figure 4.5 shows the evolution of the DES blending function for zonal-DES model ($F_{SST} = F_2$). It can be seen that after 0.8 seconds the model applies the LES model to the turbulent regions created by the slide-gate.

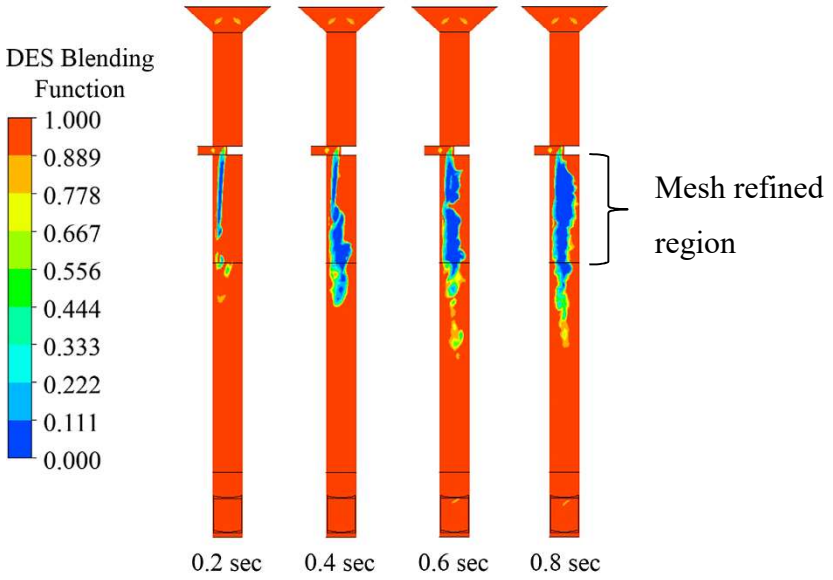

Figure 4.5. Contours of blending function at the center-plane of the nozzle; $F_{SST} = F_2$. Mesh refinement is done after the slide-gate (zonal-DES). Blue color shows areas that LES model is activated. Red and blue colors show areas where k- ε and LES models are activated, respectively.

Quality of turbulent structures is the next important feature that should be considered. An additional variable (Invariant, *I*) was defined to check this characteristic [26]:

$$I = Q^2 - S^2, \tag{2.30}$$

where Q and S are the absolute values of the vorticity and strain rate at any spatial point, respectively. Figure 4.6 presents iso-surfaces of turbulent structures inside the nozzle, where the colorbar is the viscosity ratio, the ratio of the eddy viscosity to molecular viscosity of molten steel. When the DES model does not use LES after the slide-gate, Figure 4.6(a), the model fails to predict properly the turbulent structures in that region. However, once a mesh refinement is applied after the slide-gate, Figure 4.6(b), DES is able to predict the turbulent structures, because LES is being applied in that region. Thus, the

DES model can predict turbulent structures after the slide-gate if it is calibrated appropriately.

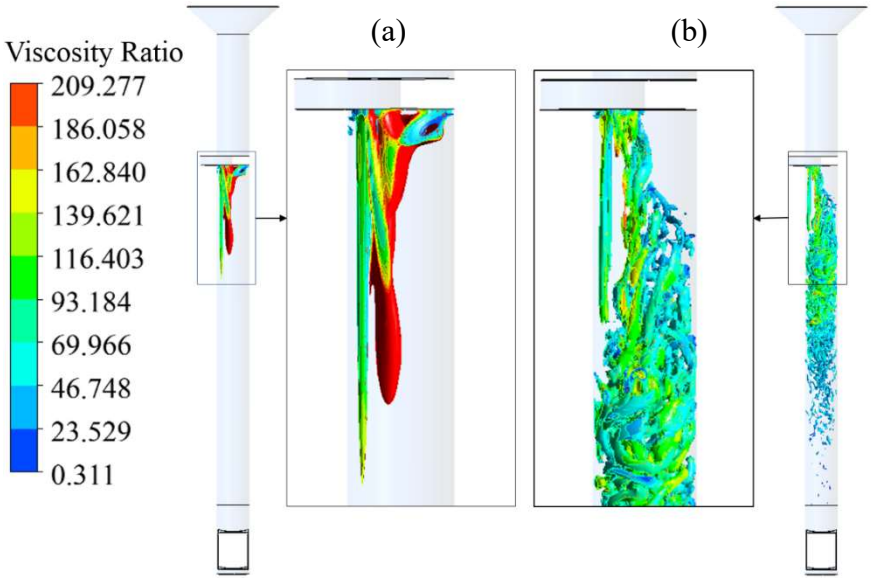

Figure 4.6. Iso-surfaces of turbulent structures after slide-gate, predicted by DES model when $F_{SST} = F_2$: (a) a uniform mesh for the entire nozzle, and (b) refined mesh after slide gate (zonal-DES, Figure 2.6). Simulation time: 2 seconds.

4.3. COMPARISON OF THREE TURBULENT MODELS (K-E, LES, AND DES)

In this section three turbulent models (k-ε, LES, and DES) have been compared together in terms of velocity profile and particle-wall interactions.

4.3.1. Velocity Profile Inside the Nozzle. Several simulations were performed using k-ε, LES, and DES models to compare the accuracy of the results in different regions of the nozzle. Figure 4.7 shows the time-averaged velocity streamlines predicted by zonal-DES and LES models, and the velocity streamlines simulated by the standard k-ε model. It can be seen that the LES and DES models are able to predict flow patterns and eddies behind the slide-gate, where the flow is separated from the surface. However, the standard k-ε model fails to simulate the flow streamlines and eddies behind the slide-gate, because it is a RANS model which cannot simulate transient turbulent structures and flow separation regions. In the nozzle out ports, since no flow separation from the surface occurs, all three models show a similar flow streamline (a flow vortex). Flow vortexes increase the particle travelling time at the nozzle out port, which can intensify particle adhesion to the walls.

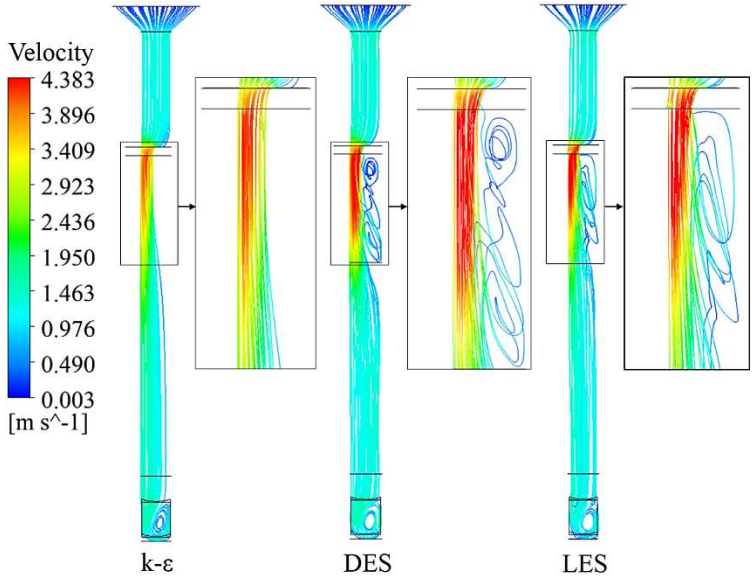

Figure 4.7. Time-averaged velocity streamlines of molten steel at the center plane of the nozzle; simulation time: 2 seconds.

The velocity profile at the nozzle centerline is also compared for k-ε, LES, and DES simulations. Figure 4.8 displays the time-averaged velocity at the centerline of the nozzle. It indicates that zonal-DES and LES models predict velocity in the entire centerline of the nozzle similarly. However, the standard k-ε model provided very different results after the slide-gate (0.26<Z<0.6), where a flow separation region occurs. The k-ε model predicts the velocity in some regions behind the slide-gate (0.3<Z<0.45) to be about 4 times higher than the velocity predicted by LES and DES models. The zonal-DES shows similar results to k-ε model at other regions where no separation is occurred. For example, at the regions where Z<0.26 and Z>0.6, zonal-DES shows similar results to k-ε model, because it switched to k-ε model in those regions.

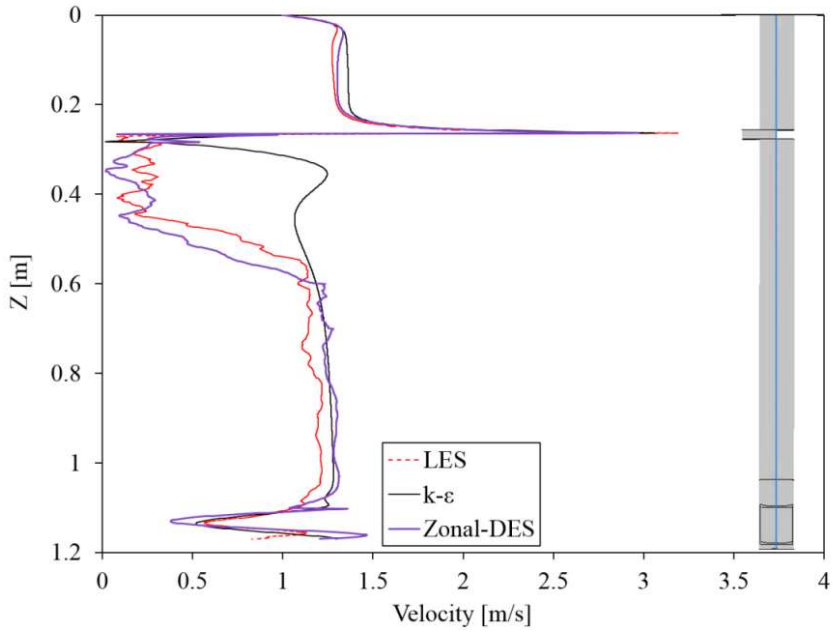

Figure 4.8. Time-averaged velocity at nozzle centerline predicted by LES, k-ε, and zonal-DES models; simulation time: 2 seconds.

4.3.2. Particle Distribution and Entrapment Inside the Nozzle. Particle distribution in the nozzle has been investigated using the LES and DES turbulent models. Figure 4.9 shows distribution of particles inside the nozzle, where the color bar shows particle velocity. The figure shows that there are regions around the slide-gate, and also at the end of the nozzle (nozzle out ports) in which particles velocity is nearly zero. In these regions, particle travelling time is higher than other regions. This phenomenon can intensify particle adhesion to the wall, because particles have more time to contact and then attach to the nozzle walls.

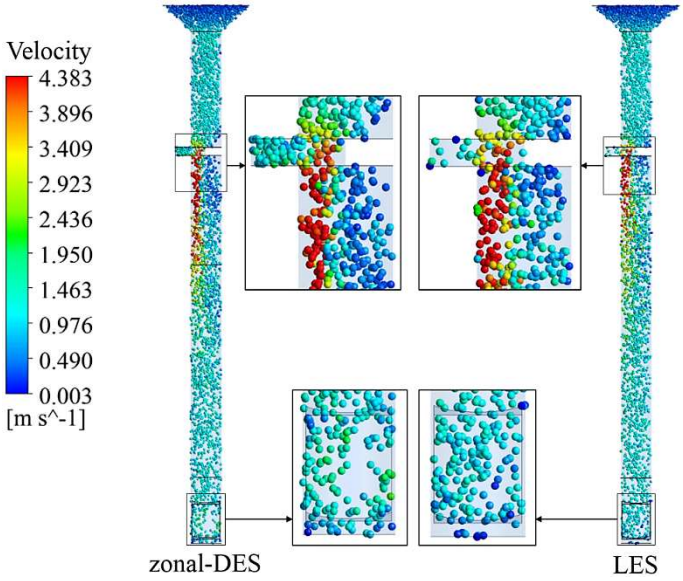

Figure 4.9. Particle distribution inside the nozzle predicted by zonal-DES and LES models; simulation time: 2 seconds. 30,000 particles per second are injected at the inlet of the nozzle. Each particle has a diameter of 50 μm. In this plot the particles are magnified for visibility.

In addition to stagnant regions, high velocity and turbulent regions also can increase particle adhesion to the wall because of turbophoresis [11], a phenomenon which takes

place in highly turbulent regions and drives particles in radial direction towards the nozzle walls.

Applying the k-ω model to the wall boundaries is one advantage of using the DES model, because k-ω is a very reliable model in simulating wall-flow interactions. Wall-particle interactions can be highlighted by assuming that every particle touching the wall will be attached to it. This assumption is helpful to determine where particles have more interaction with the nozzle walls. Figure 4.10 shows the averaged-volume fraction of attached particles on the nozzle walls after 2 seconds of simulation, predicted by LES and zonal-DES models. It is clear that a zonal-DES shows more particle-wall interactions than LES model. In high velocity regions, the thickness of viscous sub-layers decrease and the LES model has problems in simulating wall-flow interactions unless an extremely fine mesh is applied to the flow sub-layers near the nozzle walls. On the other hand, DES simulations can handle particle-wall interactions by applying a RANS model (k-ω) in regions close to the nozzle walls. That is why the volume fraction of particles attached to the wall is higher in zonal-DES.

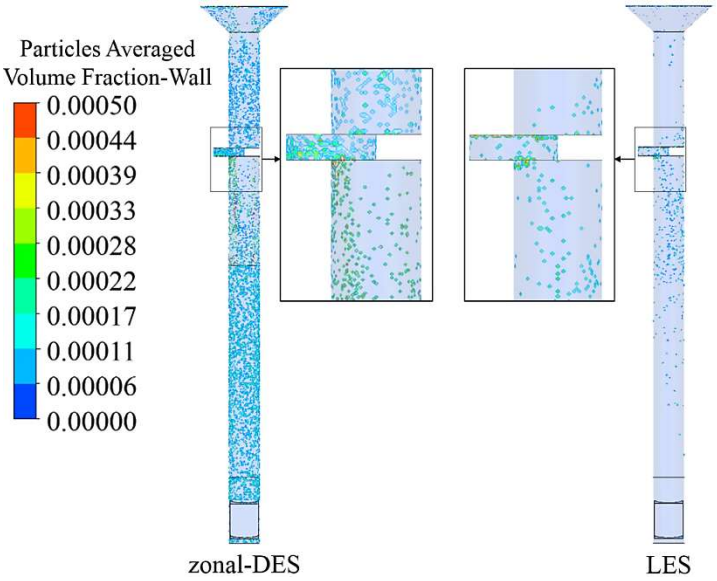

Figure 4.10. Particles averaged-volume fraction on the nozzle walls predicted by zonal-DES and LES models; simulation time: 2 seconds.

5. CONCLUSIONS

The transient simulations of molten steel flow inside a slide-gate nozzle were performed using three different turbulent models (standard k-ε, LES, and DES). The mesh convergence studies were performed to make sure the computational results were independent of the mesh size. The results indicated that zonal-DES model demands a similar number of elements and less computational time compared to the LES model, because it only applies the LES model to the flow separation regions. The calibration procedure for the DES blending function was explained in detail for the case of a slide-gate nozzle. Although the calibration procedure is complex, a calibrated DES model is able to simulate turbulent structures inside the system similar to LES model with less computational cost.

The results indicated that standard k-ε model fails to accurately simulate flow patterns after the slide-gate, where the flow is separated from the nozzle surface. DES and LES models simulate flow patterns and eddies behind the slide-gate similarly. Furthermore, the velocity profile at the centerline of the nozzle showed that zonal-DES and LES models predict similarly the velocity magnitude at the nozzle centerline. But, the k-ε model predicts a much different velocity profile through the centerline of the nozzle. In some regions after the slide-gate, k-ε predicts velocity magnitudes 4 times higher than DES and LES predictions.

Particle distribution inside the nozzle was investigated using both zonal-DES and LES models, where stagnant regions were observed around the slide-gate by both models. Stagnant regions can increase particles contact time with the nozzle surface which may intensify particle attachment onto the nozzle walls. Additionally, particle-wall interaction was studied using the assumption that every particle touching the wall will attach. It was shown that zonal-DES model predicts more particle-wall interactions compared with the LES model, because it handles the particle-wall interactions properly using a RANS model (k-ω).

REFERENCES

1. Santillana, M.B., *Thermo-mechanical properties and cracking during solidification of thin slab cast steel*. 2013: TU Delft, Delft University of Technology.

2. Yu, K.-O., *Modeling for casting and solidification processing*. 2001: CRC Press.

3. Yuan, Q., B.G. Thomas, and S. Vanka, *Study of transient flow and particle transport in continuous steel caster molds: Part I. Fluid flow.* Metallurgical and Materials Transactions B, 2004. **35**(4): p. 685-702.

4. Gheorghies, C., et al., *Theoretical model of steel continuous casting technology.* Journal of Iron and Steel Research, International, 2009. **16**(1): p. 12-16.

5. Choudhary, S. and A. Khan, *Nozzle clogging during continuous slab casting at Tata Steel.* Steel times international, 2000. **24**(3).

6. Rackers, K. and B. Thomas, *Clogging in continuous casting nozzles.* Urbana, 1995. **51**: p. 61801.

7. Zhang, L. and B.G. Thomas. *Application of Computational Fluid Dynamics to Steel Refining and Casting Processes*. in *Fourth International Conference on CFD in Oil and Gas, Metallurgical and Process Industries SINTEF, NTNU, Trondheim, Norway*. 2005.

8. Ho, Y.-H., C.-H. Chen, and W.-S. Hwang, *Analysis of molten steel flow in slab continuous caster mold.* ISIJ international, 1994. **34**(3): p. 255-264.

9. Mohammadi-Ghaleni, M., Mortaza Zivdar, and M. Nemati, *Hydrodynamic Analysis of Two Phase Separator by Computational Fluid Dynamic (CFD)*, in *6th International Conference on Advanced Computational and Experimenting*. 2012: Istanbul, Turkey.

10. Singh, R., B.G. Thomas, and S.P. Vanka, *Large Eddy Simulations of Double-Ruler Electromagnetic Field Effect on Transient Flow During Continuous Casting.* Metallurgical and Materials Transactions B, 2014. **45**(3): p. 1098-1115.

11. Ni, P., et al., *On the deposition of particles in liquid metals onto vertical ceramic walls.* International Journal of Multiphase Flow, 2014. **62**: p. 152-160.

12. Menter, F.R., *Turbulence modeling for engineering flows.* Technical Paper, ANSYS inc, 2011: p. 1-25.

13. Lucius, A. and G. Brenner, *Unsteady CFD simulations of a pump in part load conditions using scale-adaptive simulation.* International Journal of Heat and Fluid Flow, 2010. **31**(6): p. 1113-1118.

14. Yuan, Q., B.G. Thomas, and S. Vanka, *Study of transient flow and particle transport in continuous steel caster molds: Part II. Particle transport.* Metallurgical and Materials Transactions B, 2004. **35**(4): p. 703-714.

15. Fureby, C., et al., *Large eddy simulation of high-Reynolds-number wall bounded flows.* AIAA journal, 2004. **42**(3): p. 457-468.

16. Strelets, M., *Detached eddy simulation of massively separated flows*. 2001: American Institute of Aeronautics & Astronautics.

17. Bai, H. and B.G. Thomas, *Effects of clogging, argon injection, and continuous casting conditions on flow and air aspiration in submerged entry nozzles.* Metallurgical and Materials transactions B, 2001. **32**(4): p. 707-722.

18. Bai, H. and B.G. Thomas, *Turbulent flow of liquid steel and argon bubbles in slide-gate tundish nozzles: Part II. Effect of operation conditions and nozzle design.* Metallurgical and Materials Transactions B, 2001. **32**(2): p. 269-284.

19. Bai, H. and B.G. Thomas, *Turbulent flow of liquid steel and argon bubbles in slide-gate tundish nozzles: Part I. Model development and validation.* Metallurgical and Materials Transactions B, 2001. **32**(2): p. 253-267.

20. Pfeiler, C., M. Wu, and A. Ludwig, *Influence of argon gas bubbles and non-metallic inclusions on the flow behavior in steel continuous casting.* Materials Science and Engineering: A, 2005. **413**: p. 115-120.

21. Sambasivam, R., *Clogging resistant submerged entry nozzle design through mathematical modelling.* Ironmaking & steelmaking, 2006. **33**(6): p. 439-453.

22. Zhang, L., Y. Wang, and X. Zuo, *Flow transport and inclusion motion in steel continuous-casting mold under submerged entry nozzle clogging condition.* Metallurgical and Materials Transactions B, 2008. **39**(4): p. 534-550.

23. Thomas, B.G. and H. Bai. *Tundish nozzle clogging-application of computational models*. in *Steelmaking Conference Proceedings*. 2001.

24. Chaudhary, R., et al., *Transient turbulent flow in a liquid-metal model of continuous casting, including comparison of six different methods.* Metallurgical and Materials Transactions B, 2011. **42**(5): p. 987-1007.

25. Cho, S.-M., S.-H. Kim, and B.G. Thomas, *Transient Fluid Flow during Steady Continuous Casting of Steel Slabs: Part I. Measurements and Modeling of Two-phase Flow.* ISIJ international, 2014. **54**(4): p. 845-854.

26. Singh, R., B.G. Thomas, and S.P. Vanka, *Effects of a magnetic field on turbulent flow in the mold region of a steel caster.* Metallurgical and Materials Transactions B, 2013. **44**(5): p. 1201-1221.

27. Chaudhary, R., B. Thomas, and S. Vanka, *Effect of electromagnetic ruler braking (EMBr) on transient turbulent flow in continuous slab casting using large eddy simulations.* Metallurgical and Materials Transactions B, 2012. **43**(3): p. 532-553.

28. Fu, S., et al., *Simulation of wing-body junction flows with hybrid RANS/LES methods.* International Journal of Heat and Fluid Flow, 2007. **28**(6): p. 1379-1390.

29. Ivanov, N., et al., *Analysis of magnetic field effect on 3D melt flow in CZ Si growth.* Journal of Crystal Growth, 2003. **250**(1): p. 183-188.

30. Thomas, B.G. and L. Zhang, *Mathematical modeling of fluid flow in continuous casting.* ISIJ International(Japan), 2001. **41**(10): p. 1181-1193.

31. Abdilghanie, A.M., L.R. Collins, and D.A. Caughey, *Comparison of turbulence modeling strategies for indoor flows.* Journal of Fluids Engineering, 2009. **131**(5): p. 051402.

32. Menter, F. and M. Kuntz, *Development and application of a zonal DES turbulence model for CFX-5.* CFX-Validation Rep CFX-VA L, 2003. **17**.

33. Schlegel, F., et al., *Large-eddy simulation study of the effects on flow of a heterogeneous forest at sub-tree resolution.* Boundary-Layer Meteorology, 2015. **154**(1): p. 27-56.

34. Germano, M., et al., *A dynamic subgrid-scale eddy viscosity model.* Physics of Fluids A: Fluid Dynamics (1989-1993), 1991. **3**(7): p. 1760-1765.

35. Lilly, D.K., *A proposed modification of the Germano subgrid-scale closure method.* Physics of Fluids A: Fluid Dynamics (1989-1993), 1992. **4**(3): p. 633-635.

36. Nicoud, F. and F. Ducros, *Subgrid-scale stress modelling based on the square of the velocity gradient tensor.* Flow, Turbulence and Combustion, 1999. **62**(3): p. 183-200.

37. Smagorinsky, J., *General circulation experiments with the primitive equations: I. the basic experiment*.* Monthly weather review, 1963. **91**(3): p. 99-164.

38. Menter, F.R., *Two-equation eddy-viscosity turbulence models for engineering applications.* AIAA journal, 1994. **32**(8): p. 1598-1605.

39. Mahdavimanesh, M., et al., *Lagrangian Particle Tracking: Model Development.* Life Science Journal, 2013. **10**(8s).

40. Zhang, L., J. Aoki, and B.G. Thomas, *Inclusion removal by bubble flotation in a continuous casting mold.* Metallurgical and materials transactions b, 2006. **37**(3): p. 361-379.

41. Raghavendra, K., et al., *Mathematical modelling of single and multi-strand tundish for inclusion analysis.* Applied Mathematical Modelling, 2013. **37**(9): p. 6284-6300.

42. Olivieri, S., et al., *The effect of the Basset history force on particle clustering in homogeneous and isotropic turbulence.* Physics of Fluids (1994-present), 2014. **26**(4): p. 041704.

II. COMPARISON OF CFD SIMULATIONS WITH EXPERIMENTAL MEASUREMENTS OF NOZZLE CLOGGING IN CONTINUOUS CASTING OF STEELS

(Published in Metallurgical Materials Transaction B, 2016)

Mahdi Mohammadi-Ghaleni, Mohsen Asle Zaeem*, Jeffrey D. Smith, and Ronald O'Malley

Department of Materials Science and Engineering, Missouri University of Science and Technology, 1400 N. Bishop Ave, Rolla, MO 65409, USA

ABSTRACT

Measurements of clog deposit thickness on the interior surfaces of a commercial continuous casting nozzle are compared with Computational Fluid Dynamics (CFD) predictions of melt flow patterns and particle-wall interactions to identify the mechanisms of nozzle clogging. A submerged entry nozzle received from industry was encased in epoxy and carefully sectioned to allow measurement of the deposit thickness on the internal surfaces of the nozzle. CFD simulations of melt flow patterns and particle behavior inside the nozzle were performed by combining the Eulerian-Lagrangian approach and Detached Eddy Simulation (DES) turbulent model, matching the geometry and operating conditions of the industrial test. The CFD results indicated that convergent areas of the interior cross section of the nozzle increased the velocity and turbulence of the flowing steel inside the nozzle, and decreased the clog deposit thickness locally in these areas. CFD simulations also predicted a higher rate of attachment of particles in the divergent area between two convergent sections of the nozzle, which matched the observations made in the industrial nozzle measurements.

Keywords: Computational Fluid Dynamics (CFD); Detached-Eddy Simulation (DES); Continuous Casting; Submerged Entry Nozzle (SEN) Clogging; Particle-Wall Interactions.

---

* Corresponding author: Tel.: +1 573 341 7184; fax: +1 573 341 6934.

E-mail address: zaeem@mst.edu (M. Asle Zaeem).

1. INTRODUCTION

Submerged entry nozzle (SEN) clogging is a frequent but undesired phenomenon occurring in the continuous casting of steels, caused by the deposition of micro-particles/inclusions onto the interior walls of the nozzle that is used to transfer steel from the tundish to the mold [1]. Nozzle clogging has several undesired consequences, such as reducing productivity, increasing cost of casting, and decreasing quality of produced steel [2]. The quality of steel can be affected by large inclusion clusters in the final product, which are formed by inclusion attachment and buildup on the nozzle wall that can subsequently detach and be carried into the mold by the melt flow [3]. Moreover, melt flow patterns inside the nozzle, especially in the nozzle exit ports, can significantly affect flow and solidification patterns of steel inside the mold [4-7].

Computational fluids dynamics (CFD) has been the most popular method to study melt flow patterns and particle behavior in continuous casting processes, because continuous casting is an extremely high-temperature process, which makes direct experimental measurements difficult. Moreover, because of opaque nature of the nozzle, it is difficult to observe melt flow and inclusion patterns inside the nozzle [8]. Currently, CFD is a reliable and effective method to predict flow conditions and improve the efficiency of a vast variety of processes [9].

Numerous research efforts have been performed using CFD simulations to investigate the effect of melt flow and turbulence patterns on particle behavior inside the nozzle and mold [10-21]. For example, Bai et al. [10] and Zhang et al. [11] studied the effect of nozzle clogging on melt flow patterns inside the mold, where the clog layers were added to the nozzle geometry manually to study their effects on molten steel flow. Their results showed that buildup of particle clusters has a strong effect on melt flow patterns inside the nozzle and mold. By examining the effect of argon gas bubbles and inclusions on molten steel flow patterns, Pfeiler et al. [12] showed that considering two-way coupling (flow affects particle movement and vice versa) is essential for proper CFD prediction of inclusion/bubble behavior. Yuan et al. [13, 14] studied melt flow patterns, particle/inclusion distribution and capturing by the solidified front inside the mold. Their results showed that melt flow patterns and turbulence have significant influence on particle

distribution and capturing inside the mold. In 2016, Mohammadi-Ghaleni et al. [21] studied melt flow patterns, particle distribution, and particle-wall interactions inside a slide-gate nozzle using a hybrid turbulent approach. Their results showed that the hybrid method utilizing Detached Eddy Simulation (DES) can be used successfully to predict particle-wall interactions and melt flow patterns inside the nozzle, because it applies a Large Eddy Simulation (LES) model to the flow detached regions, and a Reynolds Averaged Navier-Stocks (RANS) model to layers close to the nozzle wall.

Although many researchers have investigated melt flow patterns, particle distribution, and nozzle clogging using CFD, no research has compared melt flow and turbulence patterns inside the nozzle with experimental measurements of clogging in an actual clogged nozzle. Therefore, the purpose of this paper is to compare melt flow patterns and particle adhesion to the nozzle wall, predicted by CFD simulations, with experimental measurements of clogged thickness at different cross sections of the nozzle. Accordingly, the clogged nozzle was cut in several sections, and thickness of the deposited layer on the nozzle wall was measured for every cross section. CFD simulations were performed using the DES model to determine melt flow and turbulence patterns inside the nozzle. The CFD results for melt flow patterns and particle attachment to the nozzle wall are compared with the experimentally measured thickness of clogging.

This paper includes five sections; in Sections 2 and 3, the experimental procedure and simulation approach are described, respectively. The results are presented and discussed in Section 4, and the conclusions are in Section 5.

2. EXPERIMENTAL METHODOLOGY

A SEN with internal clog deposits from a conventional slab caster that employs slide-gate flow control was received from industry to document the variations in clog deposit thickness inside the SEN. Corresponding operating data was also secured to allow CFD modeling of the process to be conducted. The clogged nozzle was encased in epoxy and carefully cut into sections to measure the thickness of deposited layer of inclusions on the nozzle wall at various locations within the nozzle, and compare these results with melt flow patterns predicted by CFD simulations. Figure 2.1 shows a schematic of the nozzle and the location of the cut sections. Cross section 1, located just below the slide-gate, was selected to investigate the effect of the flow patterns and turbulence created by the slide-gate offset on the deposition of particles in that area. Cross sections 2 and 3 were selected to examine deposition before and after the first of two convergent areas inside the nozzle bore. Similarly, cross sections 4 and 5 are situated before and after the second convergent area in the SEN. By comparing the clogging thickness in the convergent and divergent areas of the nozzle bore, we are able to investigate the influence of changes in nozzle cross section on melt flow patterns and particle deposition on the nozzle wall. The cross section 6 was selected closer to the nozzle exit ports where the bore diameter of the nozzle is constant.

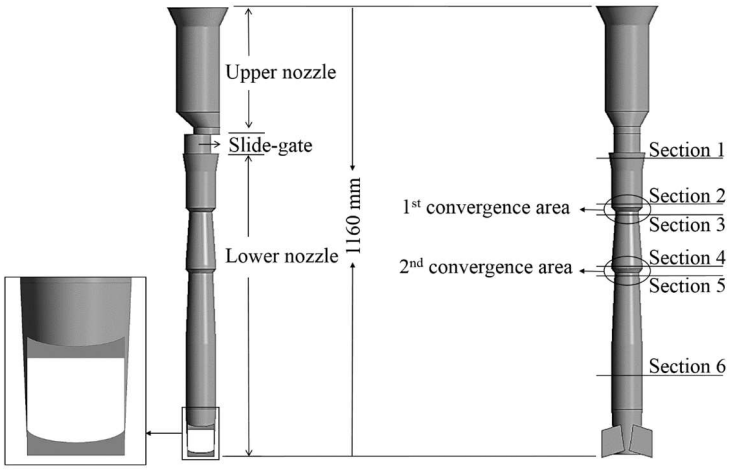

Figure 2.1. A schematic view of the nozzle and locations of cut cross sections.

3. SIMULATION APPROACH

CFD analyses were performed using ANSYS CFX 14.0. The computational domain includes a complete slide-gate nozzle consisting of upper nozzle, slide-gate, and lower nozzle. The Eulerian-Lagrangian method was used to simulate the mixture of melt flow and inclusions inside the nozzle. This method applies Eulerian approach to simulate melt flow, and Lagrangian technique to track particles inside the computational domain. To simulate flow turbulence inside the nozzle, a zonal-DES model was applied. The details of Eulerian and Lagrangian equations, DES model equations, and DES model calibration procedure can be found in Ref. [21]. Moreover, the same element size and parameters of DES model in Ref. [21] are used in this work to perform the CFD simulations. The number of elements, time step, maximum mesh size, and minimum mesh size are set to be 1.2 M, 0.0001 sec, 4 mm, and 1 mm, respectively. Figure 3.1 displays the nozzle geometry and mesh grids used for CFD simulations, and Table 3.1 presents the process parameters and information applied in the simulations.

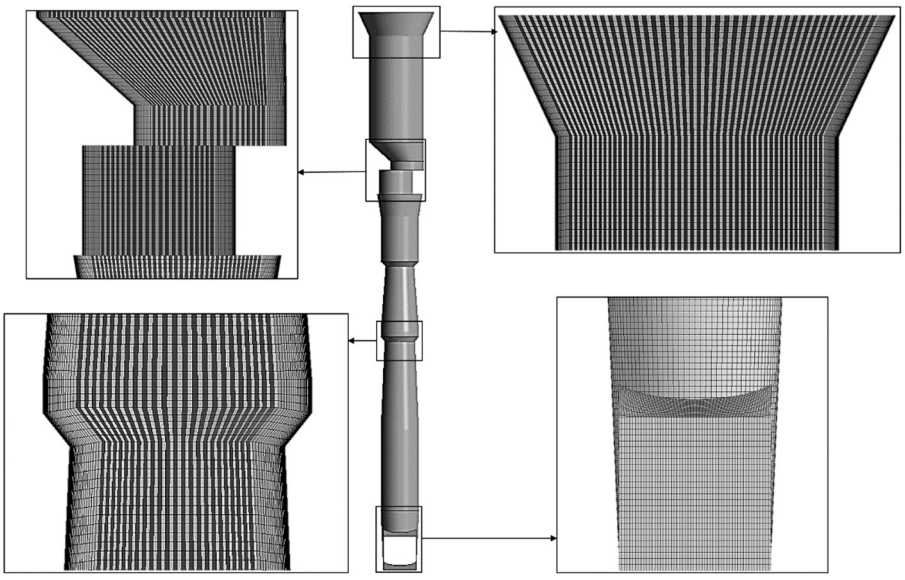

Figure 3.1. The geometry and mesh grids used for the simulations.

Table 3.1. Process parameters and information used in the simulations.

Parameter	Value	Parameter	Value
Slide-gate opening[%]	66.5	Molten steel thermal conductivity [W/m k]	41
Out ports(width × height)[mm]	70 × 70	Density of Alumina particles [kg/m^3]	4,000
Total nozzle length [mm]	1160	Number of particles	30,000
Slide-gate orientation [degree]	90	Casting temperature [K]	1,818
Viscosity of liquid steel [kg/m.sec]	0.0056	Steel thermal expansion coefficient [1/K]	0.0001
Density of liquid steel [kg/m^3]	7,021	Inlet velocity [m/sec]	From Eq. (3.1)

3.1. INITIAL AND BOUNDARY CONDITIONS

Defining proper initial and boundary conditions is very important in CFD simulations, because it directly affects accuracy of the results and convergence of the solutions. Accordingly, a uniform fully developed velocity boundary condition was assumed over the inlet of the nozzle using the following equation [14]:

$$U_{in} = U_{\max}\left(1-\frac{r}{R_{\max}}\right)^{\frac{1}{7}}, \tag{1}$$

where, U_{in} is the inlet velocity of melt flow along the nozzle inlet radius (r), $U_{\max}$ is the melt flow velocity at the center of the inlet plane ($U_{\max}$ =0.461 [m/s]), and $R_{\max}$ is the

maximum radius of the inlet plane. Additionally, turbulent kinetic energy (TKE) and dissipation rate were defined at the inlet as [21]:

$$k = 0.01 U_{in}^2 \ , \tag{2}$$

$$\varepsilon = k^{1.5} / 0.05 D \ , \tag{3}$$

where, D is the diameter of the inlet plane.

30,000 spherical particles (Al_2O_3) with the mean size of 50 microns were injected through the nozzle every second at the inlet plane. Moreover, an averaged relative pressure was applied over the exit ports of the nozzle, because part of the nozzle is submerged into the mold. Hence, the corresponding pressure at the nozzle exit ports can be defined using the following equation [21]:

$$P = \rho g h_s \ , \tag{4}$$

where ρ, g, and h_s are density of melt flow, gravity, and length of the nozzle submerged into the mold, respectively.

For initial conditions, the results of a steady state simulation were applied to the DES simulations.

4. RESULTS AND DISCUSSION

4.1. VELOCITY AND TURBULENT PROFILE INSIDE THE NOZZLE

Velocity streamlines, and TKE contours can show us an overall view of melt flow velocity and turbulence patterns in the different locations of the nozzle. Figures 4.1 and 4.2 display time-averaged velocity streamlines and TKE contours at the center plane of the nozzle, respectively. According to Figure 4.1, the time-averaged velocity profile (from view parallel to the slide-gate movement direction, view 2) is nearly symmetric. In addition, flow circulation regions are observed after the slide-gate and in the vicinity of nozzle exit ports. These regions may increase traveling time of particles inside the nozzle, which can intensify particle adhesion to the nozzle wall. Both Figures 4.1 and 4.2 indicate that the melt flow velocity and TKE increase after the slide-gate, as well as in the nozzle convergent areas. Once the melt flow velocity increases, higher forces may be imposed on inclusion clusters that are already attached to the nozzle wall, and therefor adhered inclusion clusters can be washed from the nozzle wall. Furthermore, particle adhesion to the nozzle wall can increase when TKE rises in the system because of turbophoresis, a phenomenon which occurs in highly turbulent regions that can push particles toward low turbulent regions, also radially toward the nozzle wall [21].

Tracking melt flow through the length of the nozzle also can show the magnitude of melt flow velocity and turbulence at different locations. The aim of tracking melt flow velocity and TKE inside the nozzle, especially in regions close to the walls, is to: I. understand the effect of convergent areas in the slide gate and nozzle on melt flow patterns, and II. compare melt flow patterns with experimental measurements of clog deposit thickness on the nozzle wall. For this reason, time-averaged velocity and TKE profiles along three lines through the length of the nozzle are plotted. The first line is located at the center of the nozzle (Center-line), so that the melt flow velocity at the center of the nozzle can be studied. The position of lines 2 and 3 (Left-line & Right-line), which are set to be close to the nozzle wall, can be seen at the right side of Figures 4.3 and 4.4.

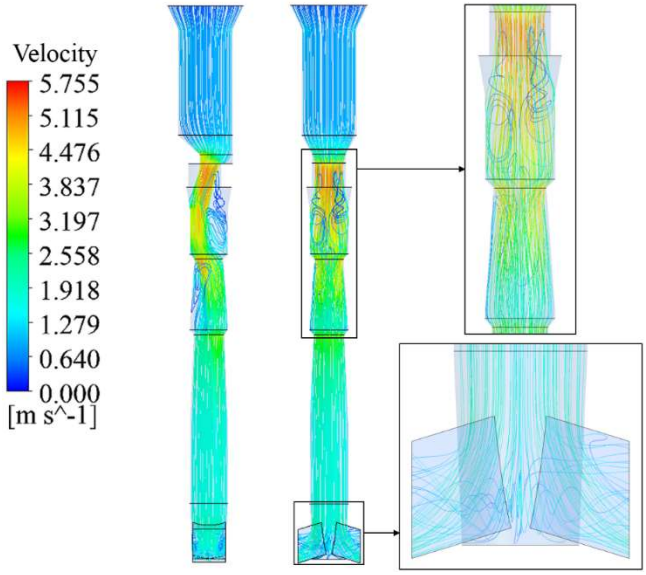

Figure 4.1. Time-averaged velocity streamlines of melt flow inside the nozzle.

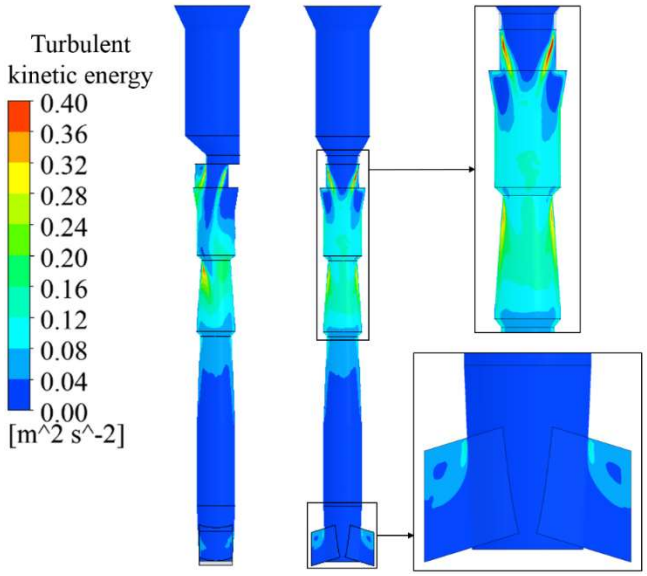

Figure 4.2. Time-averaged contours of turbulent kinetic energy contours at the center plane of the nozzle.

Figures 4.3 and 4.4 show the time-averaged velocity and TKE inside the nozzle, respectively. According to these figures, the velocity of melt flow increases in both the slide-gate and convergent areas, where the velocity and TKE peaks are located just after the slide-gate for all three lines. The last two peaks in the velocity and TKE profiles also coincide with the first and second convergent areas of the SEN bore. Moreover, according to Figure 4.3, the melt flow velocity on Left-line and Right-line become very similar after the second convergent area in the SEN bore, which suggests that the melt flow will leave the nozzle exit ports symmetrically.

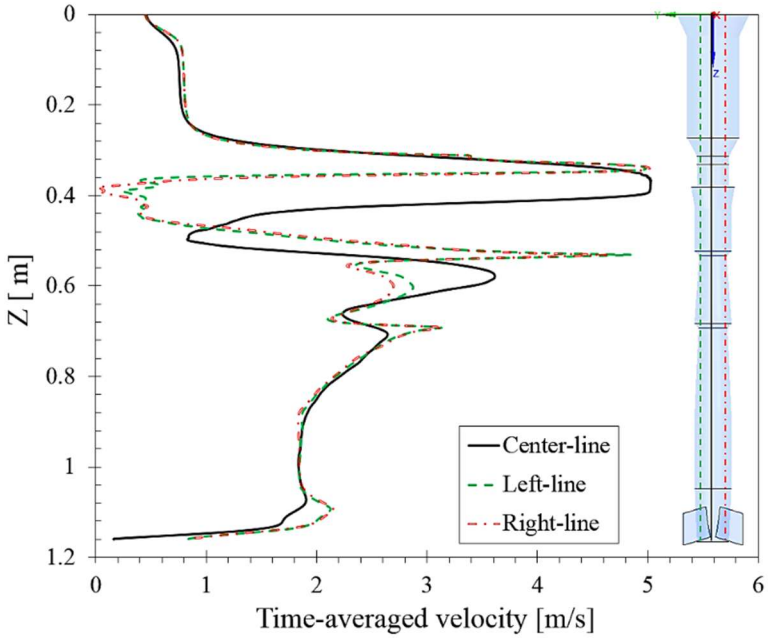

Figure 4.3. Time-averaged velocity on three lines placed inside the nozzle.

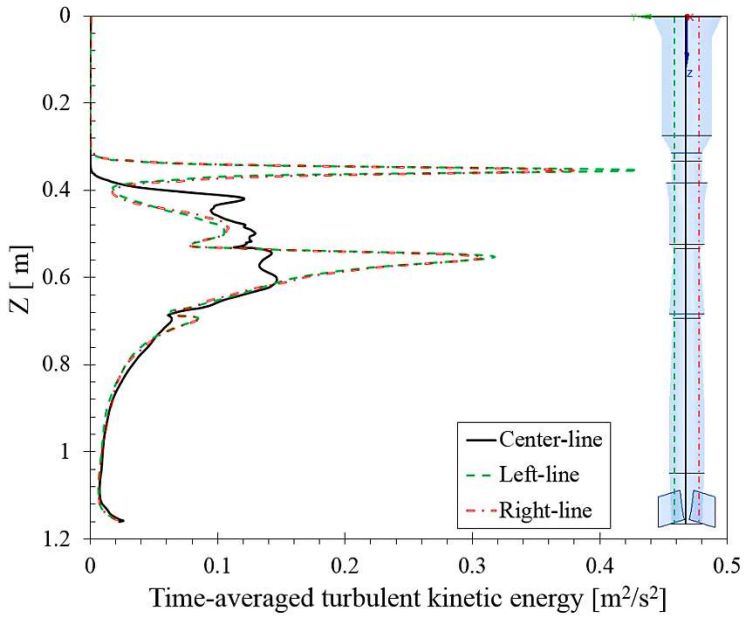

Figure 4.4. Time-averaged turbulent kinetic energy on three lines placed inside the nozzle.

4.2. COMPARING EXPERIMENTAL MEASUREMENTS AND SIMULATION RESULTS

The effect of melt flow velocity and turbulence on deposition of particles on the nozzle wall can be studied by comparing melt flow patterns with clog deposit thickness in several cross sections. Figures 4.5 to 4.10 compare angular dependence of the clog deposit thickness measurements with the time-averaged velocity and TKE contours for each cut section of the SEN. Each figure includes a drawing of the nozzle geometry with a specified cross section location on the right, a picture of the clogged nozzle cross section (a), measurements of clog deposit thickness vs radial position (b), and time-averaged velocity and TKE contours (c and d, respectively) predicted for the specific SEN cross section. In the following discussion, the results from the CFD simulation are compared with the experimental measurements for each SEN section.

Figure 4.5 is associated with section 1, which is located just below the slide-gate. Figure 4.5(a) shows that the thickest part of the wall buildup is at the open side of the slide-

gate. However, the deposited layer on this side of the slide-gate is composed entirely of solidified steel that was retained after the casting process was shut down. Ignoring this solidified steel, we observe that the particle deposition is thickest just behind the closed part of the slide-gate (90< Θ <180). Figures 4.5(c) and 4.5(d) also indicate that velocity and TKE of the melt flow increase at the open side of the slide-gate. The low velocity and TKE regions are observed just behind the close part of the slide-gate. From Figures 4.5(a) to 4.5(b), we observe that the thickest part of clog deposit is formed behind the close side of the slide-gate where low turbulent and velocity areas are observed.

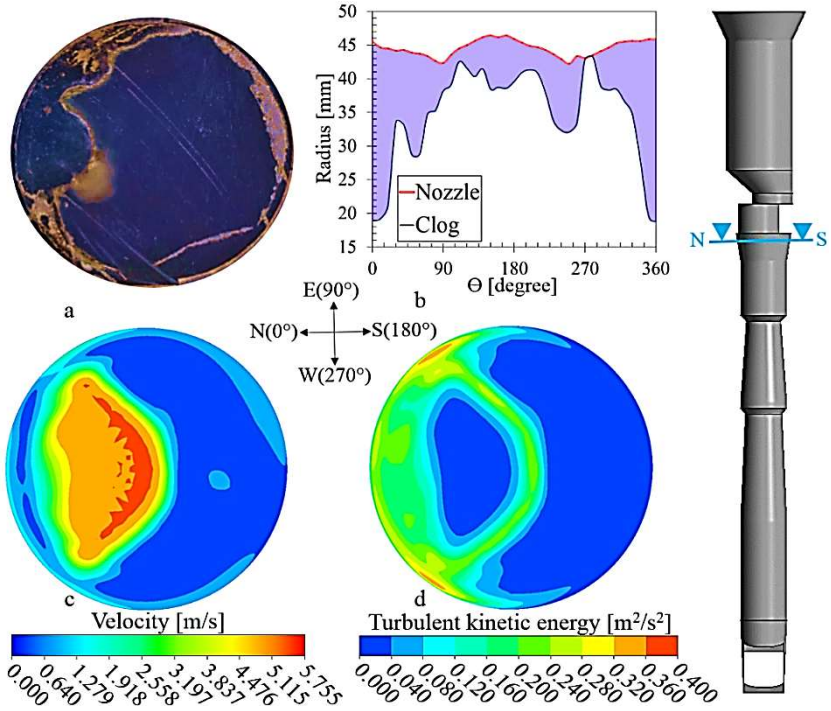

Figure 4.5. (a) Cross section 1, (b) experimental measurements of clogging thickness, (c) time-averaged velocity contours, and (d) turbulent kinetic energy contours in cross section 1.

Figure 4.6 shows cross section 2, which is located just above the first convergent area inside the nozzle. Figure 4.6 (b) shows that the clog deposit is thicker between 90 and 270 degrees (90< Θ <270) compared to the other regions where the thickness is nearly uniform. In addition, according to the Figures 4.6 (c) and 4.6 (d), the relative velocity and TKE are the lowest at 90< Θ <270. As a result, the highest clogging thickness is seen in the lowest velocity and turbulent regions for this cross section.

Figure 4.7 shows cross section 3, located just after the first convergent area in the nozzle. Figures 4.7(c) and 4.7(d) show that the convergence caused the velocity and TKE to increase inside the nozzle. Yet, the increase in TKE is not as significant as velocity. According to the Figure 4.7(a) and 4.7(b), the clog deposit is thicker between 90 and 270 degrees (90< Θ <270) than in other regions. However, compared to Figure 4.6(b), the clog deposit in Figure 4.7(b) is thinner. This suggests that once the velocity and TKE increase, the thickness of clog deposit decreases on the nozzle wall, suggesting that some of the inclusions/clusters may be detached and washed from the wall by the increase in steel flow.

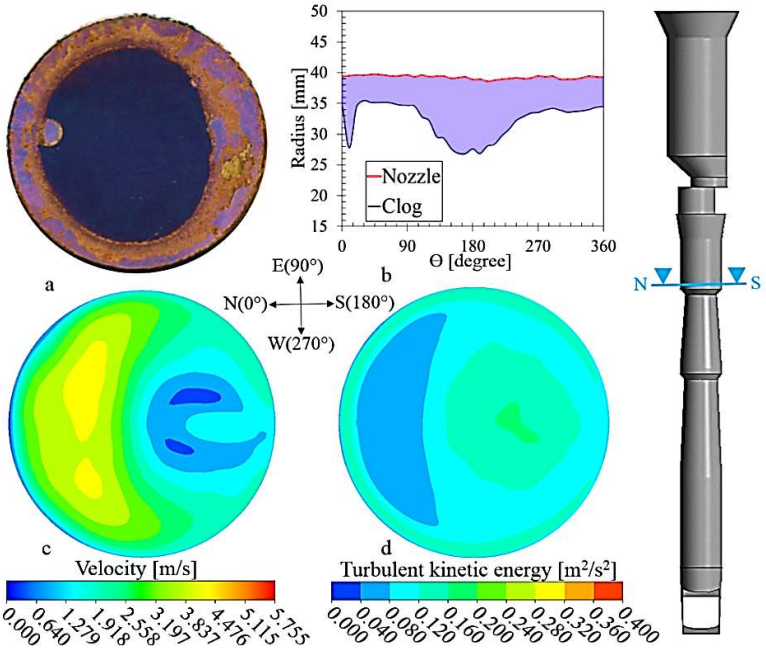

Figure 4.6. (a) Cross section 2, (b) experimental measurements of clogging thickness, (c) time-averaged velocity contours, and (d) turbulent kinetic energy contours in cross section 2.

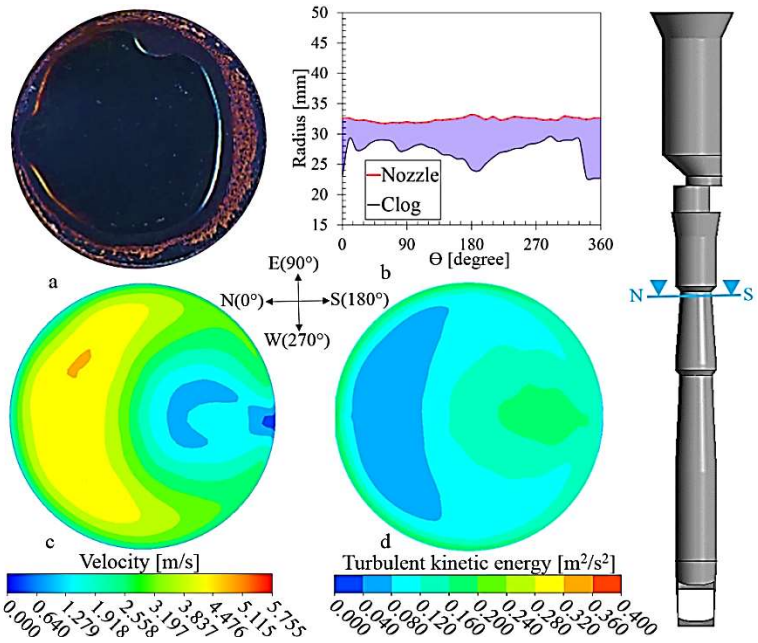

Figure 4.7. (a) Cross section 3, (b) experimental measurements of clogging thickness, (c) time-averaged velocity contours, and (d) turbulent kinetic energy contours in cross section 3.

Figure 4.8, associated with cross section 4, is located just before the second convergent area inside the nozzle. Figure 4.8(b) shows that thickness of clog deposit on the nozzle wall is nearly uniform, which can be explained by looking at velocity and TKE contours. According to the Figures 4.8(c) and 4.8(d), the velocity and TKE in section 4, close to the nozzle wall, is uniform leading to a uniform clogging thickness in this section.

Cross section 5 of the nozzle is shown in the Figure 4.9, which is located just after the second convergent area. Although some solidified steel is observed at the north (N) side of the Figure 4.9(a), the thickness of the clogging, according to Figure 4.9(b), is uniform in other regions. Moreover, Figures 4.9(c) and 4.9(d) show higher velocity and TKE in this region caused by the convergence of this area. As a result, the clog deposit is thinner in this section compared to the thickness observed in cross section 4 (Figure 4.8(a)).

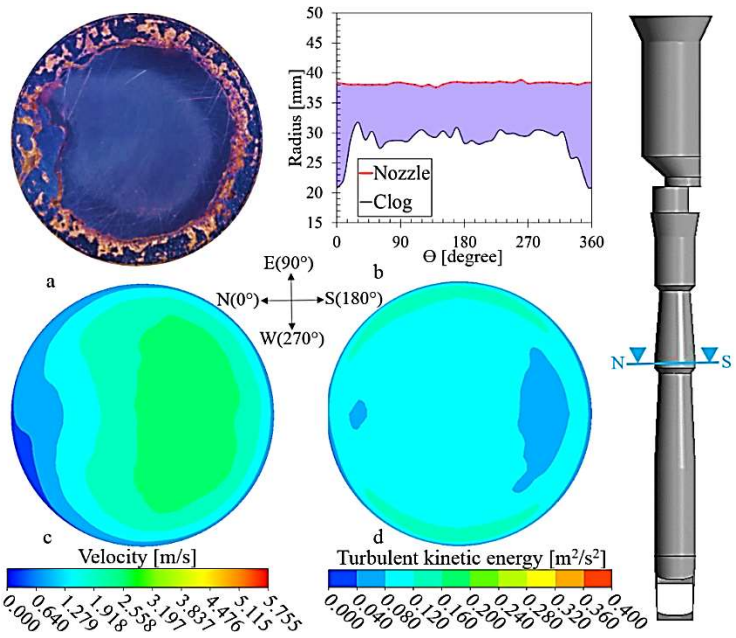

Figure 4.8. (a) Cross section 4, (b) experimental measurements of clogging thickness, (c) time-averaged velocity contours, and (d) turbulent kinetic energy contours in cross section 4.

Figure 4.10 shows cross section 6, which is located well below the second convergent area, where the nozzle bore diameter is constant along the nozzle height. The velocity and turbulent contours show uniform patterns across the nozzle cross section (Figures 4.10(c) and 4.10(d)). Hence, a nearly uniform thickness of clogging on the nozzle wall is observed in Figure 4.10 (a) and 4.10(b).

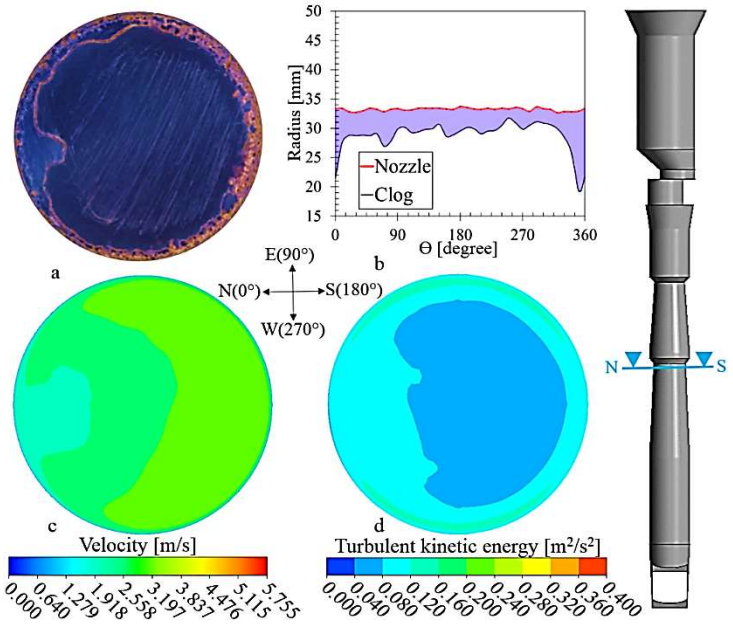

Figure 4.9. (a) Cross section 5, (b) experimental measurements of clogging thickness, (c) time-averaged velocity contours, and (d) turbulent kinetic energy contours in cross section 5.

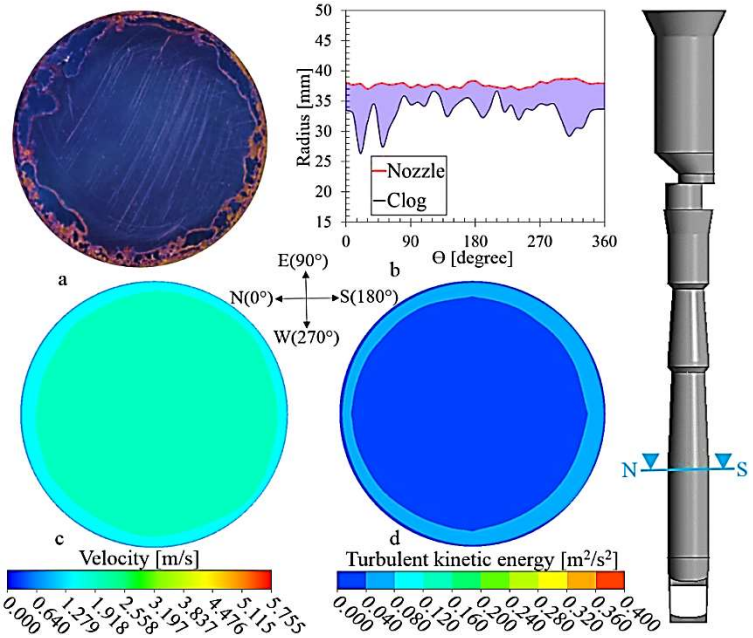

Figure 4.10. (a) Cross section 6, (b) experimental measurements of clogging thickness, (c) time-averaged velocity contours, and (d) turbulent kinetic energy contours in cross section 6.

4.2.1. Particle Deposition on the Nozzle Wall. To predict the particle-wall interactions and particle deposition on the nozzle wall, we assumed that every particle that is transported to the nozzle wall by melt flow and contacts the wall will be attached to it [21, 22]. Figure 4.11(a) shows particles inside the lower part of the nozzle (below the slide gate) after 2 seconds of simulation, where the blue particles are attached to the nozzle wall and the red particles are moving in the liquid steel. Figure 4.11(b) shows an assembly of cut sections of the nozzle from the view parallel to the slide-gate movement direction. According to this figure, clog deposit is the thickest between two convergent areas, and it decreases after the second convergent area. Likewise, Figure 4.11(a) indicates that the highest particle attachment to the nozzle wall occurs between the two convergent areas in the nozzle. Figure 4.11(a) also shows that the adhesion of particles to the nozzle wall decreases after the second convergent area, which is similar to our observations of clog deposit thickness in the industrial nozzle.

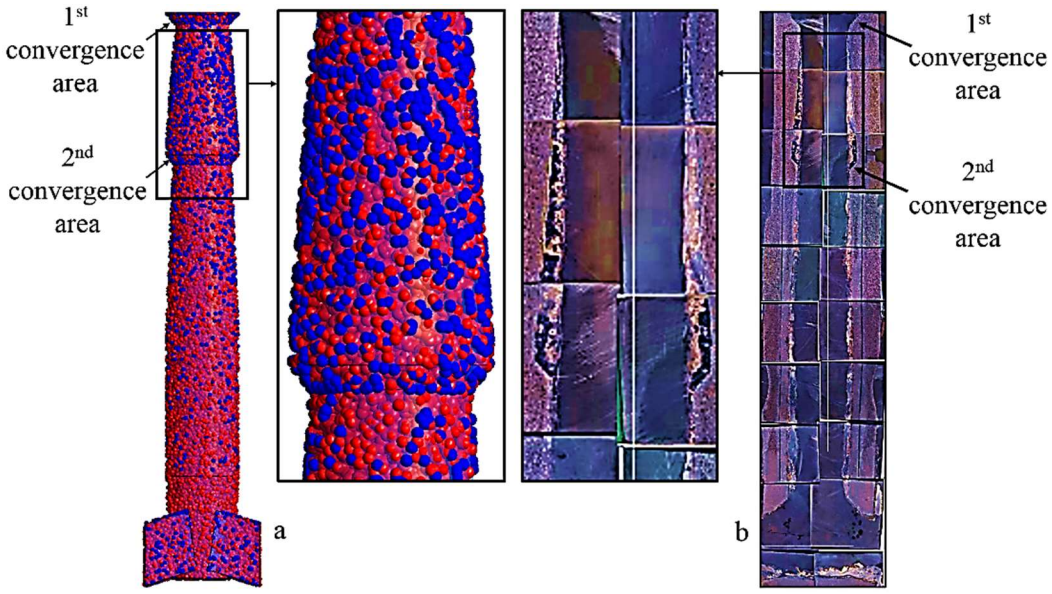

Figure 4.11. Particle deposition on the SEN walls, (a) simulations results, (b) experimental results. Only 20% of particles are shown in Figure 3.13(a) with a particle size 110 times more than their actual size for better visualization of the results.

5. CONCLUSIONS

The CFD simulations of melt flow patterns and particle adhesion to the nozzle wall were compared with measurements of clog deposit thickness in different cross sections of a clogged nozzle received from the industry. The simulations were performed using Eulerian-Lagrangian approach, and a hybrid DES turbulent model.

Streamlines of the melt velocity in the nozzle showed the flow circulation regions near the slide gate and nozzle exit ports. These regions are important because they increase traveling time of inclusions inside the nozzle. In addition, time-averaged melt flow velocity and TKE at three positions located inside the nozzle showed that the convergent areas of the nozzle increased both the velocity and the TKE of melt flow inside the nozzle. The convergent areas helped the melt flow patterns become more uniform across the nozzle cross section, which is advantageous for promoting symmetrical melt flow entering the mold.

The melt flow velocity and TKE contours were compared with thickness of clog deposits in different cut sections of the nozzle. For the first section located right below the slide-gate, a thicker clog deposit was observed behind the closed side of the slide-gate, where the velocity is low. Moreover, it was observed that the thickness of clog deposit decreased at the convergent areas of the nozzle, where the melt flow velocity increased, suggesting that inclusions may be washed from the nozzle surface because of the increased velocity. A uniform clog thickness also was observed in the areas with uniform flow patterns.

The observed clog deposit thickness was compared with results from a CFD simulation of particle adhesion to the SEN wall. The simulations were performed using the assumption that every particle that touches the wall will be attached to it. The simulation results indicated that the highest particle attachment rate to the SEN wall were in the region between the two convergent areas in the SEN bore, where the highest gradients of velocity, TKE, and irregularity of flow patterns were observed. Similarly, industrial SEN also showed the heaviest clog deposit buildup between the two convergent areas of the SEN bore.

Photographs of longitudinal sections of the SEN also showed that the clog deposits preferentially filled the divergent regions in the nozzle bore between the two convergent locations such that the inner bore diameter became nearly constant.

REFERENCES

1. Choudhary, S. and A. Khan, *Nozzle clogging during continuous slab casting at Tata Steel.* Steel times international, 2000. **24**(3): p. 21.

2. Rackers, K. and B. Thomas, *Clogging in continuous casting nozzles.* Urbana, 1995. **51**: p. 61801.

3. S. Rödl, H.S., S. Ekerot, G. Xia,N. Veneri, F. Ferro, S. Baragiola, P. Rossi, S. Fera, V. Colla, G. Bioli, M. Krings, L.-F. Sancho, A. Diaz, M. Andersson, N. Kojola, *New strategies for clogging prevention for improved productivity and steel quality*. 2008, Research Fund for Coal and Steel Unit.

4. Theodorakakos, A. and G. Bergeles, *Numerical investigation of the interface in a continuous steel casting mold water model.* Metallurgical and Materials Transactions B, 1998. **29**(6): p. 1321-1327.

5. Panaras, G., A. Theodorakakos, and G. Berggeles, *Numerical investigation of the free surface in a continuous steel casting mold model.* Metallurgical and Materials Transactions B, 1998. **29**(5): p. 1117-1126.

6. Anagnostopoulos, J. and G. Bergeles, *Three-dimensional modeling of the flow and the interface surface in a continuous casting mold model.* Metallurgical and Materials Transactions B, 1999. **30**(6): p. 1095-1105.

7. Kubo, N., et al., *Two-phase flow numerical simulation of molten steel and argon gas in a continuous casting mold.* ISIJ international, 2002. **42**(11): p. 1251-1258.

8. Ho, Y.-H., C.-H. Chen, and W.-S. Hwang, *Analysis of molten steel flow in slab continuous caster mold.* ISIJ international, 1994. **34**(3): p. 255-264.

9. Mohammadi-Ghaleni, M., Mortaza Zivdar, and M. Nemati, *Hydrodynamic Analysis of Two Phase Separator by Computational Fluid Dynamic (CFD)*, in *6th International Conference on Advanced Computational and Experimenting*. 2012: Istanbul, Turkey.

10. Bai, H. and B.G. Thomas, *Effects of clogging, argon injection, and continuous casting conditions on flow and air aspiration in submerged entry nozzles.* Metallurgical and Materials transactions B, 2001. **32**(4): p. 707-722.

11. Zhang, L., Y. Wang, and X. Zuo, *Flow transport and inclusion motion in steel continuous-casting mold under submerged entry nozzle clogging condition.* Metallurgical and Materials Transactions B, 2008. **39**(4): p. 534-550.

12. Pfeiler, C., M. Wu, and A. Ludwig, *Influence of argon gas bubbles and non-metallic inclusions on the flow behavior in steel continuous casting.* Materials Science and Engineering: A, 2005. **413**: p. 115-120.

13. Yuan, Q., B.G. Thomas, and S. Vanka, *Study of transient flow and particle transport in continuous steel caster molds: Part I. Fluid flow.* Metallurgical and Materials Transactions B, 2004. **35**(4): p. 685-702.

14. Yuan, Q., B.G. Thomas, and S. Vanka, *Study of transient flow and particle transport in continuous steel caster molds: Part II. Particle transport.* Metallurgical and Materials Transactions B, 2004. **35**(4): p. 703-714.

15. Thomas, B.G. and H. Bai. *Tundish nozzle clogging-application of computational models*. in *Steelmaking Conference Proceedings*. 2001.

16. Sambasivam, R., *Clogging resistant submerged entry nozzle design through mathematical modelling.* Ironmaking & steelmaking, 2006. **33**(6): p. 439-453.

17. Zhang, L. and B.G. Thomas, *Numerical simulation on inclusion transport in continuous casting mold.* Journal of University of Science and Technology Beijing, Mineral, Metallurgy, Material, 2006. **13**(4): p. 293-300.

18. Yuan, F., et al., *Numerical simulation of Al 2 O 3 deposition at a nozzle during continuous casting.* Journal of University of Science and Technology Beijing, Mineral, Metallurgy, Material, 2008. **15**(3): p. 227-235.

19. Lei, H., D.-Q. Geng, and J.-C. He, *A continuum model of solidification and inclusion collision-growth in the slab continuous casting caster.* ISIJ international, 2009. **49**(10): p. 1575-1582.

20. Long, M., et al., *Kinetic modeling on nozzle clogging during steel billet continuous casting.* ISIJ international, 2010. **50**(5): p. 712-720.

21. Mohammadi-Ghaleni, M., et al., *Computational Fluid Dynamics Study of Molten Steel Flow Patterns and Particle–Wall Interactions Inside a Slide-Gate Nozzle by a Hybrid Turbulent Model.* Metallurgical and Materials Transaction B, 2016: p. 1-10.

22. Ni, P., et al., *On the deposition of particles in liquid metals onto vertical ceramic walls.* International Journal of Multiphase Flow, 2014. **62**: p. 152-160.

SECTION

2. MODELING ADHESION OF PARTICLES IMPACTING A RIGID WALL IN A TURBULENT FLOW STREAM

2.1. INTRODUCTION

Nozzle clogging, caused by deposition of micro-particles (inclusions) on the nozzle wall, is a universal problem in continuous casting of steels. Nozzle clogging can cause several undesired consequences among which reducing the quality of the produced steel is the most important issue. Therefore, studying the mechanisms of adhesion of particles to the nozzle wall may help to reduce this phenomenon. In this section, we modify a general particle-wall adhesion model to be applicable in CFD simulations of turbulent flows. This model takes into account the physical and mechanical properties of both particle and wall, the effect of external forces acting on the particle, and the presence of internal forces such as surface energies of the particle and wall.

2.2. PARTICLE-WALL ADHESION MODEL

The adhesion of a spherical particle moving in a flow stream to a rigid wall depends on several significant factors such as nature of the flow stream (e.g. temperature, velocity, density etc.), particle-wall impact velocity, mechanical properties of the particle and wall, and the effect of adhesion forces (e.g. Van der Waals) at the time of contact [18-20]. These factors determine adhesion energy between particle and wall, and the particle must overcome this energy to rebound from the wall. If there is no adhesion energy, the impact is called symmetrical (the particle loses no energy during the impact). However, asymmetrical impact was observed elsewhere [21, 22], because the particle loses energy during the impact due to deformation and presence of adhesive forces (e.g. Van Der Waals). Figure 2.1 shows a schematic picture of a particle, and normal and tangent loads (P_n and P_t) imposed on the particle in contact with a vertical wall.

In Figure 2.1, M is the impulse of the wall moment, and it is taken into account to determine the rotational motion of particle during the impact. Accordingly, changes in angular momentum of particle should be equal to impulse moments [19]:

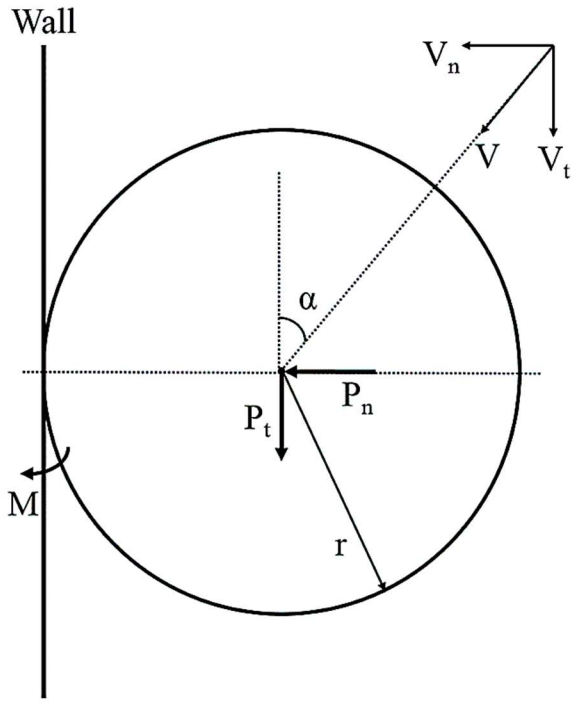

Figure 2.1. A schematic picture of a particle in contact with a vertical wall.

$$I\left(\Omega-\omega\right)=M-rP_t\ , \tag{1}$$

where, Ω and ω are rotational velocity of the particle after and before the impact, respectively. Inertia of the particle is denoted by I , and r is the particle radius. Moreover, the relation between particle rotational coefficient of restitution (the moment coefficient), e_m, and M is defined as [19]:

$$\frac{M}{I}=\frac{\left(1+e_m\right)\Omega}{e_m}\ . \tag{2}$$

The rotational coefficient of restitution can vary between -1 and 1 ($-1\le e_m\ge 1$). If $e_m\ \&\Omega=0$, the impact is totally inelastic rotationally. However, the $e_m=-1$ means that

no rotational effects occur at the contact point ($M = 0$). For this research, it is assumed that $e_m = -1$, because based on point mass impact model, the rotational energy of particle at the impact time is not significant for a wide range of micro-particles [19]. This means that all rotational velocities are equal to zero at the contact time, and $M = 0$.

Depending on the impact velocity, imposed normal load, and material properties of both particle and wall, the adhesion of a moving particle to a rigid wall can occur in four consecutive stages: I. Elastic compression stage, II. Elastic-plastic compression stage, III. Restitution stage, and IV. adhesion breakage stage [20]. The concept of these four stages will be utilized to govern the equations for normal and tangential coefficient of restitutions of the particle on the wall.

2.2.1. Elastic Compression Stage. The elastic compression stage can be described using Hertzian theory of elastic deformation [23], where all particle-wall adhesive interactions (e.g. Van Der Waals forces) are neglected. This theory assumes that the contacting bodies are isotropic, homogeneous, and the square root of contact area is small comparing to both local radius of curvature and dimension of the bodies [20, 24]. Hertzian theory provides a relationship between applied normal load (P_n), radius of contact (a), and interference distance (δ) (the distance that the spherical particle is deformed normally) [20]. Figure 2.2 displays a deformed spherical particle in contact with a rigid wall.

According to Hertzian theory, the elastic compression stage begins once the particle touches the wall ($P_n = 0$), and continues until the load reached its maximum level ($P_n = P_{\max}$), where the interference distance also is at its maximum level ($\delta = \delta_{\max}$). The Hertzian theory implies that the energy which is stored in the particle as strain energy can be determined by finding the differences of particle kinetic energy before and after elastic deformation. Hence, the formulation can be written as [20]:

$$\frac{1}{2} m v_{in}^2 - \frac{1}{2} m V_{1n}^2 = -\int_0^{\delta} P_e d\delta \ , \tag{3}$$

where, v_{in} and V_{1n} are instantaneous normal velocity of particle during the contact and particle velocity before the impact, respectively.

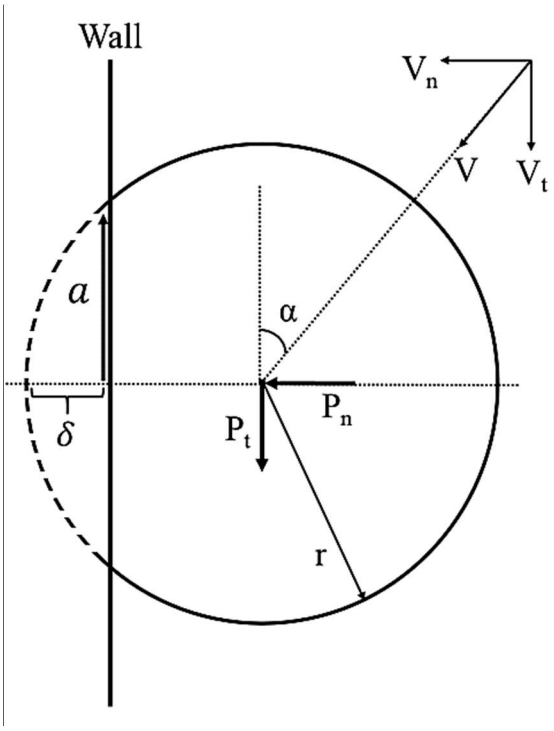

Figure 2.2. A deformed spherical particle in contact with a rigid wall.

In equation (3), P_e is the Hertzian load imposed on the particle in the elastic stage which can be defined as [24]:

$$P_e = \frac{4}{3} R^{\frac{1}{2}} \frac{E}{1-\nu^2} \delta^{\frac{3}{2}} , \tag{4}$$

where, E is the Young's modulus, ν is Poisson's ratio, and R is the radius of curvature ($R = r - \delta$). By substituting Eq. (4) is Eq. (3) and assuming $E^* = \frac{E}{1-\nu^2}$, one can write:

$$\frac{1}{2} m v_{in}^2 - \frac{1}{2} m V_{1n}^2 = -\frac{4}{3} R^{\frac{1}{2}} E^* \int_0^{\delta} \delta^{\frac{3}{2}} d\delta \ . \tag{5}$$

After integrating, Eq. (5) becomes:

$$\frac{1}{2} m v_{in}^2 - \frac{1}{2} m V_{1n}^2 = -\frac{8}{15} R^{\frac{1}{2}} E^* \delta^{\frac{5}{2}} \tag{6}$$

Rearranging Eq. (6) for V_{1n} gives:

$$V_{1n} = \left(v_{in}^2 + \frac{16}{15m} E^* R^{\frac{1}{2}} \delta^{\frac{5}{2}} \right)^{\frac{1}{2}} \ . \tag{7}$$

The maximum interference distance ($\delta_{e,\max}$) before the elastic-plastic compression starts can be defined as [25]:

$$\delta_{e,\max} = \left(\frac{\pi C Y}{2E^*} \right)^2 R \ , \tag{8}$$

where, $C = 1.295 \exp(0.736\nu)$, and Y is the yield strength. It should be noted that $CY = \min\left(\{CY\}_{wall}, \{CY\}_{particle} \right)$ [19, 20].

The maximum normal impact velocity of particle ($V_{1n,\max}$) to only elastic compression stage occurs can be derived by substituting $\delta_{e,\max}$ from Eq. (8) into Eq. (7), and assuming $v_{in} = 0$:

$$V_{1n,\max} = \left(v_{in}^2 + \frac{16}{15m} E^* R^{\frac{1}{2}} \delta_{e,\max}^{\frac{5}{2}} \right)^{\frac{1}{2}} . \tag{9}$$

Additionally, the maximum interference distance can be used to calculate the maximum load required in this stage ($P_{e,\max}$) by substituting $\delta_{e,\max}$ from Eq. (8) into Eq. (4):

$$P_{e,\max} = \frac{4}{3}\left(\frac{R}{E^*} \right)^2 \left(\frac{\pi CY}{2} \right)^3 \tag{10}$$

2.2.2. The Elastic-Plastic Compression Stage. If the impact velocity of particle be greater than maximum normal impact velocity ($V_{1n,\max} > V_{1n}$), normal load and forces imposed on the particle become greater than $P_{e,\max}$ leading to elastic-plastic compression stage start. At this point, the elastic-plastic term can be added to the Eq. (6):

$$\frac{1}{2} m v_{in}^2 - \frac{1}{2} m V_{1n}^2 = -\frac{8}{15} R^{\frac{1}{2}} E^* \delta^{\frac{5}{2}} - \int_{\delta_{e,\max}}^{\delta} P_{ep} d\delta \ , \tag{11}$$

where, P_{ep} is the elastic-plastic load defined as [20]:

$$P_{ep} = P_{e,\max} \left\{ \left[\exp\left(-\frac{1}{4}\left(\frac{\delta}{\delta_{e,\max}} \right)^{\frac{5}{12}} \right) \right] \left(\frac{\delta}{\delta_{e,\max}} \right)^{\frac{3}{2}} + \frac{4H_G}{CY} \left[1 - \exp\left(-\frac{1}{25}\left(\frac{\delta}{\delta_{e,\max}} \right)^{\frac{5}{9}} \right) \right] \frac{\delta}{\delta_{e,\max}} \right\} \tag{12}$$

where, H_G is the geometric hardness limit which depends on material properties of particle:

$$H_G = \left(2.84 - 0.92\left(1 - \cos\left(\pi \frac{a}{R} \right) \right) \right) Y \ , \tag{13}$$

where, a is the particle-wall contact radius [26]:

$$a = \sqrt{\delta R} \ . \tag{14}$$

The elastic-plastic deformation stage will continue until the interference distance reaches its maximum ($\delta = \delta_{ep,\max}$), where the plastic-elastic load is also in its maximum level ($P_{ep} = P_{ep,\max}$).

2.2.3. Restitution Stage. The restitution stage begins once the maximum elastic-plastic deformation is achieved. At this point, the particle starts to rebound, because it recovers some of the kinetic energy lost during the first two stages. However, the energy recovery is not complete, as the second deformation stage was plastic. The rebound stage continues until the particle reaches a restitution stage, where the interference length, δ , has decreased to δ_{res} . Accordingly, the radius of curvature increases to R_{res} ($R_{res} = r - \delta_{res}$).The Hertzian theory of pure elastic deformation can be applied to find the final rebound velocity since the rebound stage is assumed to be elastic [20]. Therefore, the maximum Hertzian load for the rebound stage, $P_{r,\max}$, can be determined using Eq. (4):

$$P_{ep,\max} = \frac{4}{3} R_{res}^{\frac{1}{2}} E^* \left(\delta_{ep,\max} - \delta_{res} \right)^{\frac{3}{2}} , \tag{15}$$

where, the terms $\delta_{res} - \delta_{ep,\max}$ and R_{res} can be defined as [26]:

$$\delta_{ep,\max} - \delta_{res} = \frac{3}{4} \frac{P_{ep,\max}}{E^* a_{\max}} , \tag{16}$$

$$R_{res} = \frac{4}{3} \frac{E a_{\max}}{\pi P_{ep,\max} \left(1 - \upsilon^2 \right)} , \tag{17}$$

where, $a_{\max}$ is the maximum contact radius, which can be determined using Hertzian theory [19]:

$$a_{\max} = \left[\frac{15\pi}{16} \left(\kappa_p + \kappa_w \right) r^2 m V_{1n}^2 \right]^{\frac{1}{5}} \tag{18}$$

where, $\kappa = \left(\frac{1-\upsilon^2}{\pi E} \right)$, and subscripts p and w denote particle and wall, respectively.

The maximum interference length, $\delta_{ep,\max}$, also can be determined by substituting Eq. (4.12) in Eq. (4.11) and assuming v_{in} equals to zero.

The rebound velocity of the particle in this stage, $V_{2n}^{'}$, can be used to calculate the particle coefficient of restitutions. Therefore, using Eq. (3), the rebound velocity and elastic-plastic restitution coefficient of the particle (e_{ep}) can be written as:

$$V_{2n}^{'} = \left(\frac{16}{15} E^* \right)^{\frac{1}{2}} \left(\delta_{ep,\max} - \delta_{res} \right)^{\frac{5}{4}} R_{res}^{\frac{1}{4}} \ . \tag{19}$$

$$e_{ep} = \frac{\left| V_{2n}^{'} \right|}{\left| V_{1n} \right|} \ . \tag{20}$$

Although Eq. (19) provides rebound velocity of the particle based on loss of particle kinetic energy due to two deformation stages, it does not take into account the other causes that may intensify this energy loss, such as the effect of adhesion and other forces during the contact. After the restitution stage, the particle should overcome all adhesion and external forces imposing to the contact area during the contact time to rebound from the wall.

Work of adhesion

While the particle is in contact with the rigid wall and during the deformation stages, the force of adhesion plays the most significant role in determining whether the

particle adheres to the wall or not. In the other word, particle rebounding from the wall means that a kind of work has been done to overcome adhesion forces; this kind of work is called work of adhesion. Therefore, the work of adhesion can be determined using the differences between particle rebound velocity in absence of adhesion forces and particle rebound velocity in presence of adhesion forces. In the normal direction, this relation can be written as:

$$\frac{1}{2}mV_{2n}^{2}-\frac{1}{2}mV_{2n}^{'2}=W_{An} \tag{21}$$

where, W_{An} is the work of adhesion done in normal direction. If all terms in above equation be divided by the particle normal impacting velocity (V_{1n}^{2}), the normal coefficient of restitution including the work of adhesion would be:

$$e_n=\left(e_{ep}^{2}+\frac{2W_{An}}{mV_{1n}^{2}}\right)^{\frac{1}{2}} \tag{22}$$

The Eq. (4.21) also can be written in tangential direction:

$$\frac{1}{2}mV_{2t}^{2}-\frac{1}{2}mV_{2t}^{'2}=W_{At} \tag{23}$$

where, the W_{At} is the work of adhesion in tangential direction. The tangential coefficient of restitution can be defined by dividing all terms by particle tangential impact velocity:

$$e_t=\left(e_{ep}^{2}+\frac{2W_{At}}{mV_{1t}^{2}}\right)^{\frac{1}{2}} \tag{24}$$

The Hertzian theory of deformation can be used to determine the work of adhesion [19]. Accordingly, the JKR theory of surface adhesion energy and adhesion force, F_A, are used to define the adhesion parameter of surface energy, γ [19]:

$$\gamma = \frac{2}{3}\frac{F_{Ai}}{\pi r} \tag{25}$$

where, the subscript i refers to normal and tangential velocities. Work of adhesion is defined as [19]:

$$W_{Ai} = -\frac{2}{3}\frac{a_{\max}^2 F_{Ai}}{r} \tag{26}$$

where, $a_{\max}$ is the maximum contact area radius, which can be determined using Hertzian theory [19]:

Therefore, using Eq. (25) and (26), the work of adhesion can be defined as:

$$W_{Ai} = -\left[\frac{5}{4}\rho\pi^{\frac{9}{2}}\left(\kappa_p + \kappa_w\right)\right]^{\frac{2}{5}} \gamma r^2 \left|V_{1i}\right|^{\frac{4}{5}} \tag{27}$$

According to Eq. (25), the adhesion force can be used to find the adhesion energy parameter. The adhesion force can be sum of several kinds of forces acting on the contact area during contact time. These forces can be individually significant depending on the nature of the process. The adhesion force for a particle moving inside a flow stream can be written as sum of different forces [19, 27]. Hence, the normal and tangential adhesion forces (F_{An} and F_{At}) for our case can be defined as:

$$F_{An} = F_{vdw} + F_{dn} \tag{28}$$

$$F_{At} = F_{vdw} + F_{dt} + F_b + F_g \tag{29}$$

In above equations, F_{vdw} is the Van Der Waals force:

$$F_{vdw} = \frac{h a_m^2}{8\pi z^3} \ , \tag{30}$$

where, h is the Van Der Waals constant, and z is adhesion distance that occurs between the wall and particle during the deformation stages.

F_{di} is the normal drag force per unit particle mass defined as:

$$F_{di} = \frac{9\mu}{2r^2\rho_p}\frac{C_d Re_p}{24} V_{fi} \ , \tag{31}$$

where, ρ_p is particle density, and C_d *, and* Re_p are drag coefficient, and particle Reynolds number, respectively. V_{fi} is the flow stream velocity in the i direction.

$$C_d = \begin{cases} \frac{24}{\mathrm{Re}}\left(1+\frac{1}{6}\mathrm{Re_p}^{2/3}\right) & \text{if } \mathrm{Re_p}<1000 \\ 0.44 & \text{if } \mathrm{Re_p}\geq 1000 \end{cases} , \tag{32}$$

$$\mathrm{Re}_P = \frac{2r\rho_f \left|V_{fi}\right|}{\mu_f} \ , \tag{33}$$

where, Re and ρ_f are the flow stream Reynolds number and density, respectively.

F_b is the buoyancy force due to the difference between the density of flow stream and particle:

$$F_b = \frac{4\pi r^3}{3}\left(\rho_p - \rho_f\right) g \tag{34}$$

F_g is the gravity force acting on the particle:

$$F_G = \frac{\rho_p - \rho}{\rho} g \quad , \tag{35}$$

There exist other forces that could be considered in the equations for calculating the adhesion force (e.g. capillary (F_{cap}), image (F_i), and contact potential forces (F_{cp}) [19]). However, the significance of any mentioned forces may vary depending on the nature of the process we are dealing with. For example, for the case of micro particles moving in the molten steel flow stream (our case), Van der Waals, gravity, drag, and buoyancy should be considered to be the most important forces acting during the contact time [19, 27]. Therefore, only the forces mentioned are considered to calculate the particle-wall adhesion force in this research.

3. CONCLUSIONS AND FUTURE WORKS

3.1. CONCLUSIONS

CFD simulations of molten steel flow patterns and particle-wall interactions inside the nozzles of continuous casting process were performed using a hybrid turbulent model, Detached Eddy Simulations (DES). The results showed that the DES model has both advantages of LES and RANS model in transient wall-bounded simulations. The convergence areas of the nozzle increased the velocity and turbulence, and decreased the clog deposit thickness locally in these areas. CFD simulations predicted a higher rate of attachment in the divergent area between two convergent sections of the nozzle, which matched the observations made in the industrial nozzle measurements. A Particle-wall adhesion model also was provided to be applicable in Lagrangian CFD simulations.

3.2. FUTURE WORK

It is recommended to CFD simulations of melt flow patterns inside the nozzle using the hybrid turbulent approach (DES) be compared with the experimental measurements. Also, the proposed model for particle-wall adhesion (chapter 4) can be added to the CFD simulations and compare the results with the experimental measurements of nozzle clogging in chapter 3. In addition, the effect of different parameters such as argon injection, size of particles, different level of input velocity turbulence, and geometrical edition of the nozzle can be considered in the future studies.

REFERENCES

1. Santillana, M.B., *Thermo-mechanical properties and cracking during solidification of thin slab cast steel*. 2013: TU Delft, Delft University of Technology.

2. Gheorghies, C., et al., *Theoretical model of steel continuous casting technology.* Journal of Iron and Steel Research, International, 2009. **16**(1): p. 12-16.

3. Lukavaya, M. and G. Mikhailov, *Factors affecting the clogging of submerged nozzles during continuous casting of steel.* Russian Metallurgy (Metally), 2008. **2008**(8): p. 698-699.

4. Long, M., et al., *Kinetic modeling on nozzle clogging during steel billet continuous casting.* ISIJ international, 2010. **50**(5): p. 712-720.

5. Zhang, L. *Fluid Flow, Heat Transfer and Inclusion Motion In Molten Steel Continuous Casting Tundishes*. in *Fifth International Conference on CFD in the Process Industries*. 2006. Melbourne.

6. Yu, K.-O., *Modeling for casting and solidification processing*. 2001: CRC Press.

7. Yuan, Q., B.G. Thomas, and S. Vanka, *Study of transient flow and particle transport in continuous steel caster molds: Part I. Fluid flow.* Metallurgical and Materials Transactions B, 2004. **35**(4): p. 685-702.

8. Choudhary, S. and A. Khan, *Nozzle clogging during continuous slab casting at Tata Steel.* Steel times international, 2000. **24**(3).

9. Takei, K. and F. Lindén Bergman, *Clogging Prevention in Submerged Entry Nozzles Focusing on CaTiO3 as a Coating Material.* 2012.

10. Memarpour, A., *An Experimental Study of Submerged Entry Nozzles (SEN) Focusing on Decarburization and Clogging*. 2011, Royal Institute of Technology: Stockholm.

11. Sakalli, E., *Nozzle blockage in continuous casting of Al-killed sea 1006 and sea 1008 steel grades in iskenderun iron and steel works*. 2004, The Middle East Technical University.

12. Jeklene, O., *Optimization of the quality of continuously cast steel slabs using the firefly algorithm.* Materiali in tehnologije, 2011. **45**(4): p. 347-350.

13. Rackers, K. and B. Thomas, *Clogging in continuous casting nozzles.* Urbana, 1995. **51**: p. 61801.

14. Thomas, B.G. and H. Bai. *Tundish nozzle clogging-application of computational models*. in *Steelmaking Conference Proceedings*. 2001.

15. Ho, Y.-H., C.-H. Chen, and W.-S. Hwang, *Analysis of molten steel flow in slab continuous caster mold.* ISIJ international, 1994. **34**(3): p. 255-264.

16. Mohammadi-Ghaleni, M., *Simulation of a two-phase separator by Computational Fluid Dymanics (CFD)*, in *The department Chemical Engineering*. 2012, University of Sistan and Baluchestan: Zahedan, IRAN.

17. *ANSYS Fluent User Manual*. 2006, ANSYS Inc.

18. Wall, S., W. John, and S.L. Goren, *Application of impact adhesion theory to particle kinetic energy loss measurements*, in *Particles on Surfaces 2*. 1989, Springer. p. 19-34.

19. Brach, R.M. and P.F. Dunn, *A mathematical model of the impact and adhesion of microsphers.* Aerosol Science and Technology, 1992. **16**(1): p. 51-64.

20. Singh, S. and D. Tafti. *Predicting the Coefficient of Restitution for Particle Wall Collisions in Gas Turbine Components*. in *ASME Turbo Expo 2013: Turbine Technical Conference and Exposition*. 2013. American Society of Mechanical Engineers.

21. Brenner, S., H. Wriedt, and R. Oriani, *Impact adhesion of iron at elevated temperatures.* Wear, 1981. **68**(2): p. 169-190.

22. Rogers, L. and J. Reed, *The adhesion of particles undergoing an elastic-plastic impact with a surface.* Journal of Physics D: Applied Physics, 1984. **17**(4): p. 677.

23. Hertz, H., *Miscellaneous papers*. 1896: Macmillan.

24. Campbell, C.S., *Granular material flows–an overview.* Powder Technology, 2006. **162**(3): p. 208-229.

25. Jackson, R., I. Chusoipin, and I. Green, *A finite element study of the residual stress and deformation in hemispherical contacts.* Journal of tribology, 2005. **127**(3): p. 484-493.

26. Etsion, I., Y. Kligerman, and Y. Kadin, *Unloading of an elastic–plastic loaded spherical contact.* International Journal of Solids and Structures, 2005. **42**(13): p. 3716-3729.

27. Mohammadi-Ghaleni, M., et al., *Computational Fluid Dynamics Study of Molten Steel Flow Patterns and Particle–Wall Interactions Inside a Slide-Gate Nozzle by a Hybrid Turbulent Model.* Metallurgical and Materials Transaction B, 2016: p. 1-10.

VITA

Mahdi Mohammadi-Ghaleni was born in Iran. He completed both bachelor's and master's degrees in Chemical Engineering on 2008 and 2012, respectively, before moving to US. on January 2014.

Mahdi started his research as a graduate research assistant in the department of Materials Science and Engineering (MSE) at Missouri University of Science and Technology (Missouri S&T) to work on CFD simulations of melt flow patterns and nozzle clogging in continuous casting of steels. During his graduate studies at Missouri S&T, he, in addition to one conference talk and poster presentation, published two journal papers in Metallurgical and Materials Transactions B. During his last semester at Missouri S&T, Summer 2016, Mahdi worked for ArcelorMittal Global R&D as Research Engineer-Intern.

Mahdi was a member of Material Advantage and Alpha Sigma Mu honor society, and received three scholarships during his studies at Missouri S&T. He also served Council and Graduate Students (CGS) in Missouri S&T as the representative of Materials Science and Engineering department for two years. Mahdi received his master's degree in Materials Science and Engineering from Missouri University of Science and Technology in December 2016.